Slip rate and locking depth from GPS profiles across the southern Dead Sea Transform

Maryline Le Beon,[1] Yann Klinger,[1] Abdel Qader Amrat,[2] Amotz Agnon,[3] Louis Dorbath,[4] Gidon Baer,[5] Jean-Claude Ruegg,[1] Olivier Charade,[1] and Omar Mayyas[2]

Received 20 July 2007; revised 1 June 2008; accepted 25 July 2008; published 6 November 2008.

[1] The Dead Sea Transform is a major strike-slip fault bounding the Arabia plate and the Sinai subplate. On the basis of two GPS campaign measurements, 6 years apart, at 17 sites distributed in Israel and Jordan, complemented by Israeli permanent stations, we compute the present-day deformation across the southern segment of the Dead Sea Transform, the Wadi Araba fault. Elastic locked-fault modeling of fault-parallel velocities provides a slip rate of 4.9 ± 1.4 mm/a and a best fit locking depth of ~12 km. This slip rate is slightly higher than previous results based only on Israeli permanent GPS stations data, which are located west of the fault. It is in good agreement with results based on offset geomorphologic and geologic features that average longer periods of time (10 ka to 1 Ma). Projection in ITRF2000 reference frame allows using our data, combined with results published earlier, to further study the kinematics between Arabia, Nubia, and Sinai. Systematic combination of Euler poles available in the literature, in addition to our new set of data, shows that a wide range of Arabia-Sinai pole positions and angular velocities predict reasonable slip rate on the Dead Sea fault. We highlight uncertainties of calculating such poles due to the small size of the blocks and their slow relative motion along a short and almost straight strand of the transform fault, which lead to a large trade-off between pole location and angular velocity.

Citation: Le Beon, M., Y. Klinger, A. Q. Amrat, A. Agnon, L. Dorbath, G. Baer, J.-C. Ruegg, O. Charade, and O. Mayyas (2008), Slip rate and locking depth from GPS profiles across the southern Dead Sea Transform, *J. Geophys. Res.*, *113*, B11403, doi:10.1029/2007JB005280.

1. Introduction

[2] The Dead Sea Transform (DST), also known as the Levant fault system, accommodates the northward motion of Arabia, on the east, relative to the Sinai subplate on the west (Figure 1). This left-lateral strike-slip fault, about 1000 km long, connects the Red Sea mid-oceanic ridge to the south to the continental collision zone of Caucasus to the north, where the DST joins with the East Anatolian fault. Other boundaries of the Sinai subplate remain poorly known, although the Gulf of Suez exhibits little deformation and continuous seismic activity, attesting to the existence of a tectonic boundary with Nubia there [*Garfunkel and Bartov*, 1977; *Bosworth and Taviani*, 1996; *Salamon et al.*, 1996, 2003; *Mahmoud et al.*, 2005; *Riguzzi et al.*, 2006].

[3] On the basis of geologic observations, 105 km of left-lateral motion in total has been documented along the southern part of the fault, south of Dead Sea, since the fault initiated 15 to 20 Ma ago [*Quennell*, 1958; *Freund et al.*, 1968, 1970; *Garfunkel*, 1981; *Courtillot et al.*, 1987]. However, the rate at which the fault accommodates horizontal displacement is still a matter of debate, as published values vary between 2 and 10 mm/a (Table 1). Although knowledge on historical and archeological seismic history is among the best in the world [*Ambraseys et al.*, 1994; *Ellenblum et al.*, 1998; *Meghraoui et al.*, 2003; *Guidoboni et al.*, 1994, 2004; *Marco et al.*, 2005; *Daëron et al.*, 2005, 2007; *Agnon et al.*, 2006; *Elias et al.*, 2007], direct and conclusive long-baseline geodetic measurement of the slip rate has not been published.

[4] Until recently, the present-day deformation across the DST remained poorly constrained. Starting in 1996, permanent GPS stations have been progressively installed in Israel, that allow to estimate the slip rate from short GPS profiles across the southern part of the fault [e.g., *Wdowinski et al.*, 2004] and to include the Sinai subplate in regional plate motion models [e.g., *Reilinger et al.*, 2006]. This network, however, includes only two stations east of the fault and thus the GPS profiles do not account for the entire plate boundary deformation.

[5] In this study we provide a direct measurement of the current slip rate along the DST based on three dense campaign-style GPS profiles across the southern part of the fault, the Wadi Araba fault (Figure 1). Profile locations

[1]Equipe de Tectonique, Institut de Physique du Globe de Paris, CNRS, Paris, France.
[2]Seismology Division, Natural Resources Authority, Amman, Jordan.
[3]Institute of Earth Sciences, Hebrew University of Jerusalem, Jerusalem, Israel.
[4]Ecole et Observatoire des Sciences de la Terre, Strasbourg, France.
[5]Geological Survey of Israel, Jerusalem, Israel.

0148-0227/08/2007JB005280$09.00

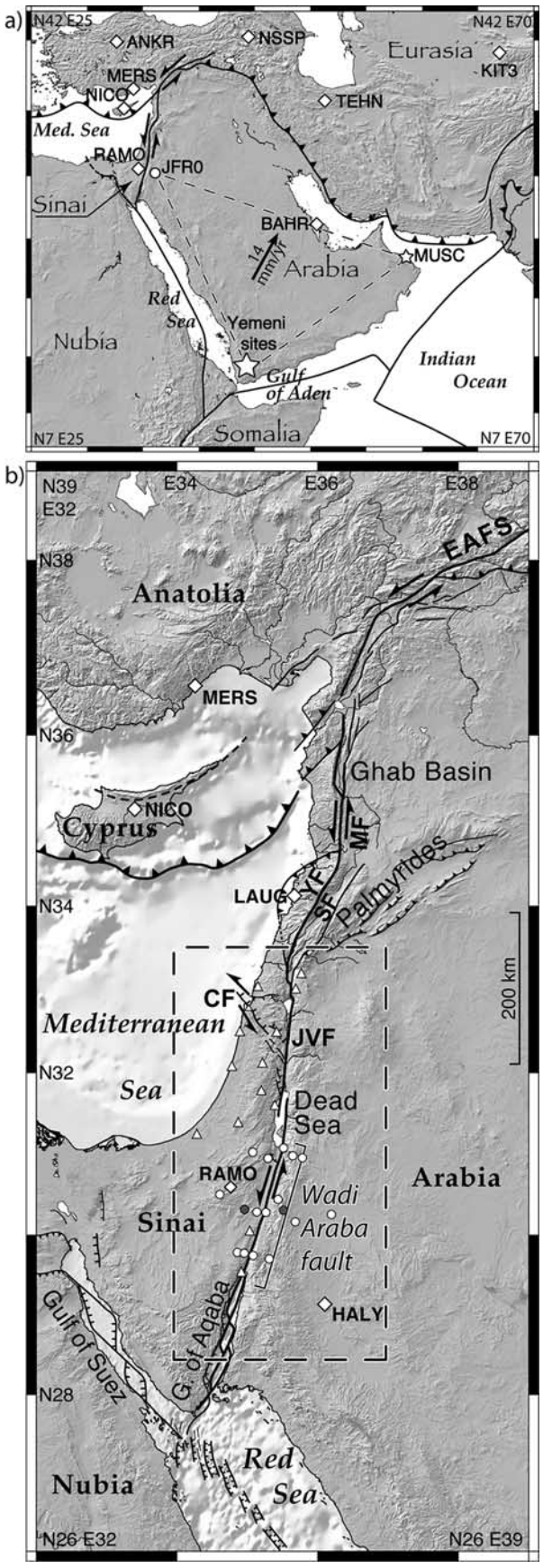

have been chosen to take advantage of the simple linear geometry of the plate boundary [*Garfunkel*, 1981] (Figure 1) and of the possibility to anchor benchmarks far enough from the fault, in the nondeforming part of the tectonic plate, on both sides of the fault. An elastic locked fault model [*Savage and Burford*, 1973] is used to interpret the observed deformation in term of slip rate along the DST. Secondarily, we use a combination of our data and published GPS results for the Arabia plate to compute Euler vectors of the Arabia and Sinai blocks in ITRF2000 and to further investigate the relative motion between Arabia, Sinai, and Nubia plates. Varying results associated to large uncertainties are discussed in relation to geometry and relative motion of the tectonic blocks.

2. Data Acquisition and Processing

[6] A GPS network of 17 sites was installed and surveyed twice, in October 1999 and March 2005. It is distributed along three profiles perpendicular to the Wadi Araba fault (Figure 1b). Benchmarks consist of 10-cm steel nails strongly glued in holes drilled in bedrock. Dual-frequency Ashtech Z12 and ZX receivers and Ashtech choke ring antennas were used during both campaigns. The sites have been occupied for 48 to 72 h with a sampling interval of 30 s during each campaign, except sites MAP0 and QUL0 (Figure 1b) that were occupied continuously during both campaigns and site BUR0, measured only 8 h in 1999. A rolling network of six receivers was operating simultaneously at any time during the campaign, in addition to the Israeli permanent stations, insuring that station positions could be determined through several short baselines. Data of 20 to 30 permanent stations (Table 2) from the Israeli network (GIL) and the International GPS Service (IGS), located around the study area, were also included to complement our network and to link the campaign data to a global reference system. In addition to regular processing, calculations spanning 6 to 8 days were also run for permanent stations at epochs 2002.11, 2004.47, and 2006.32, in order to better constrain their velocities and to include new sites as the Israeli network evolves. Epochs have been chosen to optimize the number of Israeli stations and of key regional IGS stations (such as BAHR, for example) available and

Figure 1. Tectonic setting of our study area. (a) Tectonic boundaries of the Arabia plate. Slip vector is derived from *Vigny et al.* [2006] Euler vector of Arabia relative to Nubia. Dashed lines underline triangular geometry at the scale of Arabia plate defined by the sites used to determine Arabia rotation parameters. Med. Sea, Mediterranean Sea. (b) Tectonic map of the Dead Sea Transform. Mapping of faults is modified from *Daëron et al.* [2004] and *Elias et al.* [2007]. EAFS, East Anatolian fault system; CF, Carmel fault; JVF, Jordan Valley fault; YF, Yammouneh fault; SF, Serghaya fault; MF, Missyaf fault. Box shows location of Figure 5. We locate on both figures some GPS data included in our study: diamonds stand for IGS sites, circles for campaign sites (gray circles are sites MAP0 and QUL0, observed permanently during each campaign), triangles for Israeli permanent stations and stars for data published by *Vigny et al.* [2006].

Table 1. Selected Previous Estimates of Slip Rate Along the Dead Sea Transform

Slip Rate	Time Span	Method[a]	Reference
3.7 ± 0.4	~5 years	Direct GPS measurement, south Lebanon	*Wdowinski et al.* [2004]
4–5	~4 years	Direct GPS measurement, Lebanon	*Gomez et al.* [2007]
4.4 ± 0.3	~10 years	Large-scale GPS data, Wadi Araba	*Reilinger et al.* [2006]
6.9 ± 0.1	2 ka	Paleoseismology, Syria	*Meghraoui et al.* [2003]
5.1 ± 1.3[b]	25 ka	Offset alluvial fans, YF, Lebanon	*Daëron et al.* [2004]
1.4 ± 0.2[b]	10 ka	Paleoseismology, offset channels, SF, Lebanon	*Gomez et al.* [2003]
4 ± 2	10–100 ka	Offset alluvial fans, Wadi Araba	*Klinger et al.* [2000b]
5.25 ± 2.25	2–5 Ma	Offset alluvial fans, Wadi Araba	*Ginat et al.* [1998]
8.5 ± 1.5	~5 Ma	Geological offsets, south Lebanon	*Freund et al.* [1968]
>5.8	<18 Ma		*Garfunkel* [1981]

[a]YF, Yammouneh fault; SF, Serghaya fault (Figure 1).
[b]Total left-lateral slip rate in Lebanon should be the sum of the YF and SF slip rates.

providing good quality data. When possible, we also favored epochs close to the period of the year we did our measurements in order to minimize possible impact of seasonal effects on our data.

[7] We analyzed the phase observations using the GAMIT/GLOBK software package [*Herring*, 1999; *King and Bock*, 2000]. In the first step, LC observables (i.e., dual frequency) were computed using precise orbits calculated by IGS [*Beutler et al.*, 1993] and fixing ambiguities to integer values for baselines shorter than 500 km. Seven tropospheric delay parameters per day were estimated, and IGS tables were used to model antenna phase center variations. This step resulted in precise baseline components and estimates of positions for each day. To assess the quality of the processing, we plot the baseline components repeatability to represent the scattering of daily solutions around their mean value. Figure 2 shows that for 100-km-long baselines, typical of our network, the mean scattering of the results is about 1 mm for the north component and about 2 mm for the east component, both in 1999 and 2005. Figure 2 also provides maximum values of the weighted root-mean-square deviation (WRMS) for the longest baselines of our network. They reach about 4 and 7 mm for the north and east components, respectively.

[8] Next, using GLOBK, we combined our loosely constrained daily GAMIT solutions with daily data processed by SOPAC (http://sopac.ucsd.edu/dataArchive), which include more than 100 stations located all over the world, using a six-parameter Helmert transformation (rotation and translation). This resulted in a global-scale network of precise baselines for each campaign. To assess the quality of the processing at this step, we estimated station positions for each day and for each campaign, by fitting, in the least square sense, the positions of 25 stations from the International Terrestrial Reference Frame 2000 (ITRF2000) database [*Altamimi et al.*, 2002] listed in Table 3. Daily and long-term position time series (see examples in Figure 3) were examined at that step to detect outliers. In order to obtain accurate positions and velocities, the baseline solutions of each period were then combined together and projected into ITRF2000 by adjusting both positions and velocities of 25 fiducial stations to their ITRF2000 value. Position and velocity misfits relative to ITRF2000 are 7.4 mm and 1.3 mm/a, respectively, indicating that the velocity field is properly projected into ITRF2000 reference frame (see *Vigny et al.* [2006] and *Vernant et al.* [2004] for comparison). Table 3 summarizes position and velocity in

Table 2. Permanent GPS Sites Included in the GAMIT Processing at Each Epoch[a]

Site	1999.8	2002.1	2004.6	2005.2	2006.3
Campaigns	x	-	-	x	-
ANKR	x	x	x	x	x
AREL	-	-	-	**x**	**x**
ARTU	x	x	x	x	x
BAHR	x	x	x	x	x
BSHM	x	x	x	x	x
CAGL	x	x	x	-	x
CSAR	-	-	-	**x**	**x**
DAKA	-	-	-	x	x
DRAG	**x**	**x**	**x**	**x**	**x**
EBRE	x	x	x	x	x
ELAT	**x**	**x**	**x**	**x**	**x**
ELRO	-	-	**x**	**x**	**x**
GILB	**x**	**x**	**x**	**x**	**x**
GRAS	x	x	x	x	x
GRAZ	x	x	-	-	x
HALY	-	-	x	x	-
JOZE	x	x	x	x	x
JSLM	-	-	**x**	**x**	**x**
KABR	**x**	**x**	**x**	**x**	**x**
KATZ	**x**	**x**	-	**x**	**x**
KIT3	-	x	x	x	-
LAMP	x	x	x	x	x
LAUG	-	-	x	x	x
LHAV	-	-	**x**	**x**	**x**
MALI	x	x	x	x	x
MAS1	x	x	x	x	x
MATE	x	x	x	x	x
MERS	-	x	-	x	x
METS	x	x	x	x	x
NAMA	-	-	-	x	-
NICO	x	x	x	x	x
NKLG	-	x	x	x	x
NRIF	-	-	-	**x**	**x**
NSSP	-	-	x	x	-
POL2	x	x	x	x	x
POTS	x	x	x	x	x
RABT	-	x	x	x	x
RAMO	x	-	x	x	x
SLOM	-	-	**x**	**x**	**x**
SOFI	x	x	x	x	-
SOLA	-	-	x	x	-
TEHN	-	-	-	x	x
TELA	**x**	**x**	**x**	**x**	**x**
WSRT	x	x	x	x	x
WTZR	x	x	x	x	x
ZECK	x	x	x	x	-
ZIMM	x	-	-	-	-

[a]Cross stands for stations included, dash stands for stations not included. Bold indicates stations from the Israeli network. RAMO, located in southern Israel, is an IGS station.

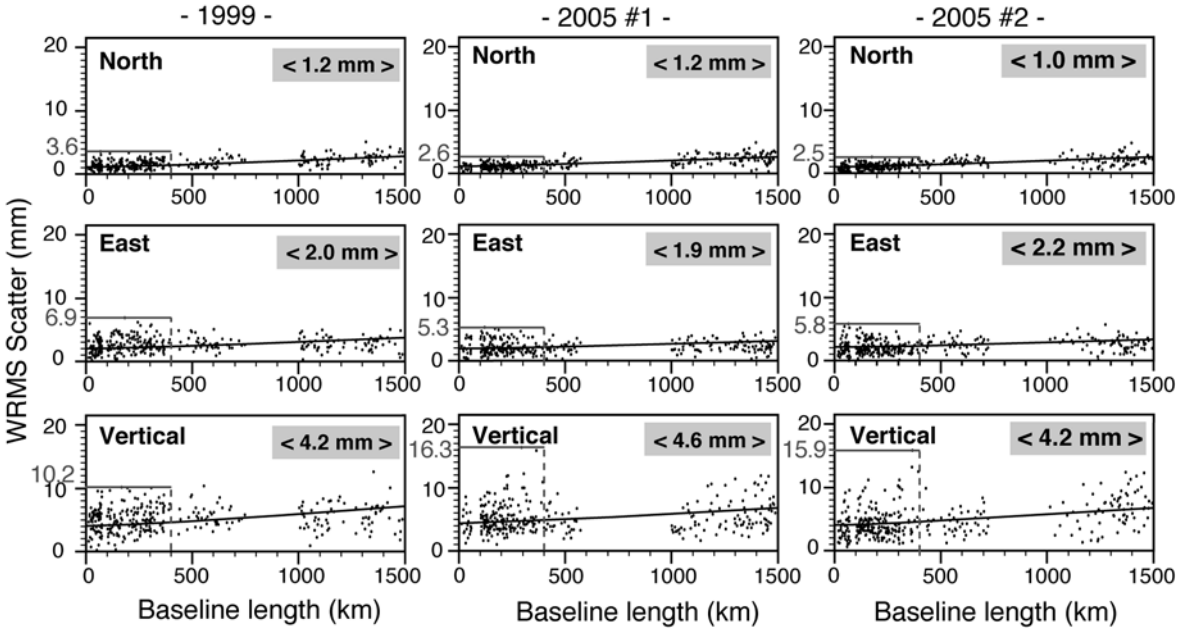

Figure 2. Repeatability of baseline components for the processing of the 1999 and 2005 data sets. Because of limited size of the matrices, GAMIT processing for the 2005 data set had to be separated in two parts that share a large number of common stations, both local and regional. Vertical axis represents the scattering of daily solutions around their mean value. Curve shows average dispersal. Numbers in gray rectangle are average dispersal for the 100-km-long baselines, representative of our campaign network. The repeatability values suggest good quality of the data and of the processing. We also indicate the maximum scattering for the longest baselines between local stations, 400 km.

ITRF2000 for all stations considered in this study. Several permanent stations (AREL, CSAR, DAKA, HALY, NRIF, NSSP, SOLA, SLOM) had to be discarded because of low measurement repeatability or apparent position instability.

[9] GPS processing software are known to underestimate calculated uncertainties (<0.5 mm/a) [e.g., *Feigl et al.*, 1993; *Langbein and Johnson*, 1997; *Williams et al.*, 2004; *Reilinger et al.*, 2006; *Vigny et al.*, 2006]. When processing continuous GPS data, appropriate models of noise can be applied, which is not possible for campaign data processing. The baselines repeatability provides an estimate of the uncertainty on relative positions for each campaign (Figure 2). Hence, we estimate the uncertainty on the relative velocities, which also depends on the time between successive measurements. For our campaign sites, maximum velocity uncertainty would be 0.8 and 1.6 mm/a for the north and east component, respectively. To reach these more realistic uncertainties on the velocities, we added random walk Markov noise (imaging the monument instability) of amplitude 2 mm/$\sqrt{}$a when combining daily solutions with GLOBK, as commonly done when processing campaign-style GPS data (see references above). We obtain uncertainties of about 1 mm/a for the campaign sites (Table 3). Slightly smaller uncertainties are obtained for permanent stations as we determined up to five solutions within 6.5 years. When the time interval between the measurements is only 2 years, the error bars are larger, 1.3 to 1.8 mm/a (e.g., sites JSLM and LHAV). Because the two campaigns occurred at the end of October and at mid-March, our data may be affected by seasonal variations, recorded by long-term time series of continuous stations [e.g., *Wdowinski et al.*, 2004; SOPAC, http://sopac.ucsd.edu/cgi-bin/refinedJavaTimeSeries.cgi]. Between the two epochs considered in this study, the amplitude of such variations has negligible effect on the velocity.

[10] Although the velocities determined at the campaign sites are based only on two measurements, uncertainties appear to be low, largely due to the fact that the time interval between the two campaigns is 5.6 years. These results remain, however, very sensitive to the accuracy of the measurements in 1999 and 2005 and should be interpreted carefully. We further discuss this issue in section 3.

3. Velocity Field and Slip Rate Along Dead Sea Fault Segment

3.1. Defining an Arabia Fixed Reference Frame

[11] In order to study the relative motion between Arabia and Sinai, we choose to represent our data relative to stable Arabia, rather than stable Sinai, because rigid rotation of Arabia is better defined (Table 4, section 5). We considered the Arabia-fixed reference frame obtained by subtracting the rotation of Arabia from the velocity field, in ITRF2000, newly computed from our measurements. The only stations considered in stable Arabia, JFR0 (located in Jordan, 90 km east of the DST) and BAHR (Bahrain) (Figure 1a), provide too limited data to determine accurately the parameters of the rigid rotation for the Arabian plate. They were complemented by other GPS data acquired in southern Arabia by *Vigny et al.* [2006] (Figure 1a), the only abundant data set in ITRF2000 available in the literature. Given the different processing strategies of the two teams, we paid

Table 3. GPS Station Positions and Horizontal Velocities in ITRF2000 and Relative to Arabia[a]

			ITRF2000		Fixed Arabia			
Site	Longitude	Latitude	V_e	V_n	V_e	V_n	σV_e	σV_n
				Arabia				
ABK0	**35.27**	**30.28**	**25.0**	**20.9**	**−0.1**	**−2.4**	**1.05**	**1.03**
AYN0	**35.78**	**30.96**	**24.2**	**22.8**	**−0.6**	**−0.7**	**1.04**	**1.01**
BAHR	50.61	26.21	31.6	28.7	0.6	0.3	0.98	0.91
BUR0	**35.64**	**30.98**	**23.0**	**24.7**	**−1.7**	**1.2**	**1.17**	**1.21**
ELRO[b]	35.77	33.18	23.3	21.6	0.1	−1.8	1.8	1.78
JEM0	**35.08**	**29.75**	**24.4**	**23.3**	**−1.1**	**0.1**	**1.05**	**1.01**
JFR0	**36.19**	**30.26**	**25.0**	**23.1**	**−0.4**	**−0.6**	**1.06**	**1.00**
KATZ[b]	35.69	33.00	22.9	20.6	−0.4	−2.9	0.93	0.91
MAN0	**35.68**	**30.17**	**24.7**	**23.2**	**−0.6**	**−0.2**	**1.05**	**1.01**
QUL0	**35.51**	**30.31**	**25.7**	**21.7**	**0.5**	**−1.7**	**0.99**	**0.96**
ROM0	**35.31**	**29.70**	**26.3**	**22.0**	**0.8**	**−1.3**	**1.05**	**1.01**
SAF0	**35.52**	**31.08**	**23.8**	**21.3**	**−0.8**	**−2.1**	**1.05**	**1.02**
SUL0	**35.44**	**30.44**	**23.8**	**22.8**	**−1.2**	**−0.6**	**1.11**	**1.07**
				Sinai				
BOR0	**34.61**	**30.51**	**23.9**	**18.6**	**−1.0**	**−4.5**	**1.02**	**0.99**
BSHM[b]	35.02	32.78	21.9	18.8	−1.4	−4.4	0.91	0.88
DIM0	**35.08**	**31.03**	**24.0**	**17.5**	**−0.5**	**−5.7**	**1.02**	**0.99**
DRAG[b]	35.39	31.59	23.2	19.0	−1.0	−4.4	0.94	0.91
ELAT[b]	34.92	29.51	25.7	20.2	0.1	−2.9	0.93	0.9
GILB[b]	35.42	32.48	22.8	20.0	−0.8	−3.3	0.92	0.88
JSLM[b]	35.20	31.77	23.8	16.7	−0.2	−6.5	1.29	1.21
KABR[b]	35.15	33.02	21.9	18.6	−1.2	−4.6	0.92	0.88
LAUG	35.67	34.12	21.2	19.5	−1.2	−4.0	1.81	1.78
LHAV[b]	34.87	31.38	23.1	18.3	−1.2	−4.8	1.85	1.83
MAP0	**34.97**	**30.32**	**23.1**	**20.1**	**−2.0**	**−3.1**	**0.99**	**0.96**
MNH0	**35.13**	**30.29**	**25.0**	**18.9**	**−0.1**	**−4.3**	**1.04**	**1.01**
RAMO	34.76	30.60	23.5	18.2	−1.4	−4.8	0.92	0.88
SAG0	**34.86**	**29.78**	**24.8**	**19.3**	**−0.6**	**−3.8**	**1.04**	**1.00**
TAM0	**35.30**	**30.95**	**24.9**	**18.5**	**0.2**	**−4.8**	**1.02**	**0.99**
TELA[b]	34.78	32.07	22.7	18.1	−1.0	−5.0	0.91	0.88
TIM0	**34.96**	**29.78**	**25.5**	**19.6**	**0.1**	**−3.6**	**1.03**	**1.00**
				Africa				
HRAO[c]	27.69	−25.89	19.6	17.7	−29.5	−2.4	1.07	0.97
LAMP[c]	12.61	35.50	20.9	17.1	3.8	4.3	0.89	0.83
MALI	40.19	−3.00	26.5	15.6	−16.8	−9.5	1.48	1.05
MAS1[c]	344.37	27.76	16.8	15.8	−5.6	18.6	0.94	0.86
RABT	353.15	34.00	16.5	16.3	−0.4	14.1	1.36	1.15
SUTH[c]	20.81	−32.38	18.0	20.7	−32.5	3.8	1.16	1.04
				America				
ALGO[c]	281.93	45.96	−15.2	2.1	−35.6	32.1	1.01	0.93
CHUR[c]	265.91	58.76	−17.6	−3.0	−36.4	29.2	0.95	0.93
DUBO[c]	264.13	50.26	−17.4	−4.5	−42.4	27.8	0.94	0.9
GODE[c]	283.17	39.02	−15.1	3.0	−39.7	32.7	0.97	0.89
PIE1[c]	251.88	34.30	−14.2	−7.4	−51.5	24.7	0.97	0.89
				Australia				
CEDU[c]	133.81	−31.87	27.0	58.1	5.0	39.3	0.96	0.86
DARW[c]	131.13	−12.84	34.7	57.8	−0.9	37.7	1.52	1.21
PERT[c]	115.89	−31.80	38.0	57.1	12.2	31.0	0.97	0.88
				Eurasia				
ANKR	32.76	39.89	0.0	11.5	−17.4	−10.7	0.92	0.87
ARTU[c]	58.56	56.43	24.5	5.3	10.7	−25.0	0.9	0.87
CAGL	8.97	39.14	22.9	14.5	9.3	3.6	0.95	0.89
EBRE	0.49	40.82	20.7	14.3	9.5	8.1	0.98	0.91
GLSV[c]	30.50	50.36	23.1	11.5	14.9	−9.8	1.00	0.93
GRAS	6.92	43.76	21.6	14.6	12.4	4.8	0.93	0.89
GRAZ	15.49	47.07	22.6	13.4	15.1	−0.9	0.97	0.93
IRKT[c]	104.32	52.22	22.3	−8.1	−14.4	−37.5	1.29	1.14
JOZE[c]	21.03	52.10	21.1	12.9	16.9	−4.1	0.92	0.85
MATE[c]	16.70	40.65	24.2	17.4	10.8	2.5	0.87	0.82
MERS	34.26	36.57	13.5	14.7	−6.8	−8.2	1.13	1.08
METS	24.40	60.22	20.7	11.2	22.7	−7.4	0.94	0.91
NICO[c]	33.40	35.14	19.4	13.8	−1.7	−8.7	0.86	0.82
ONSA[c]	11.93	57.40	18.1	12.9	20.6	0.4	0.96	0.93
POL2[c]	74.69	42.68	27.7	4.4	−1.6	−27.9	0.92	0.87
POTS	13.07	52.38	20.1	13.5	17.8	0.4	0.92	0.9
SELE[c]	77.02	43.18	28.3	2.6	−1.6	−29.8	1.00	0.95

Table 3. (continued)

Site	Longitude	Latitude	ITRF2000		Fixed Arabia			
			V_e	V_n	V_e	V_n	σ V_e	σ V_n
SOFI[c]	23.40	42.56	24.4	11.1	11.4	−7.0	0.91	0.83
URUM[c]	87.60	43.81	30.4	6.6	−3.3	−25.5	1.18	1.08
WSRT	6.61	52.92	18.4	14.6	17.6	5.0	0.93	0.9
WTZR[c]	12.88	49.14	21.2	13.9	16.0	0.9	0.87	0.85
ZECK[c]	41.57	43.79	26.1	10.2	9.4	−15.4	0.96	0.91

[a]Bold indicates the campaign stations. Velocities are given in mm/a. Uncertainties are 1σ level. V_e and V_n are east and north components of velocity, respectively.
[b]Israeli permanent stations.
[c]Stations used for projection in ITRF2000.

special attention to the consistency between the different ITRF2000 realizations. Hence, the misfit between the 14 common fiducial stations used in both studies (see Table 3 of this study and Table 2 of *Vigny et al.* [2006]) is 1.6 mm/a, with especially good agreement at BAHR (residue of 0.1 mm/a), demonstrating that merging the two data sets is meaningful.

[12] Finally, seven stations were used to determine the rigid rotation of Arabia: BAHR, JFR0, and five stations from *Vigny et al.* [2006], located in Oman (MUSC) and Yemen (DHAM, HODD, JNAR, and SANA). These stations are distributed according to a very appropriate geometry as they define a triangle at the scale of the whole plate (Figure 1). The location of JFR0, closer to the pole of rotation compared to other stations, strongly constrains the definition of the pole. Because the four Yemeni stations all lie close to each other, at the southern tip of Yemen, they were weighted half the normal value to avoid possible bias during the inversion process. Station KHAS, located onshore Hormuz Strait and part of *Vigny et al.*'s [2006] data set, was discarded due to its proximity to the Zagros-Makran transition zone [e.g., *Berberian and King*, 1981; *Byrne et al.*, 1992; *Vernant et al.*, 2004; *Regard et al.*, 2005]. Hence, the Euler vector for the Arabia plate with respect to ITRF2000 (Table 4) is N52.53, E349.36 and Ω = 0.479 ± 0.015°/Ma, with RMS< 1.6 mm/a at each station considered (Figure 4). The Euler vector departs only slightly from the solution published earlier by *Vigny et al.* [2006] (Table 4) to take into account the new data at JFR0: the rotation is slightly faster with the pole located accordingly more to the east. This Euler vector, however, differs significantly from the Euler vector proposed by *Sella et*

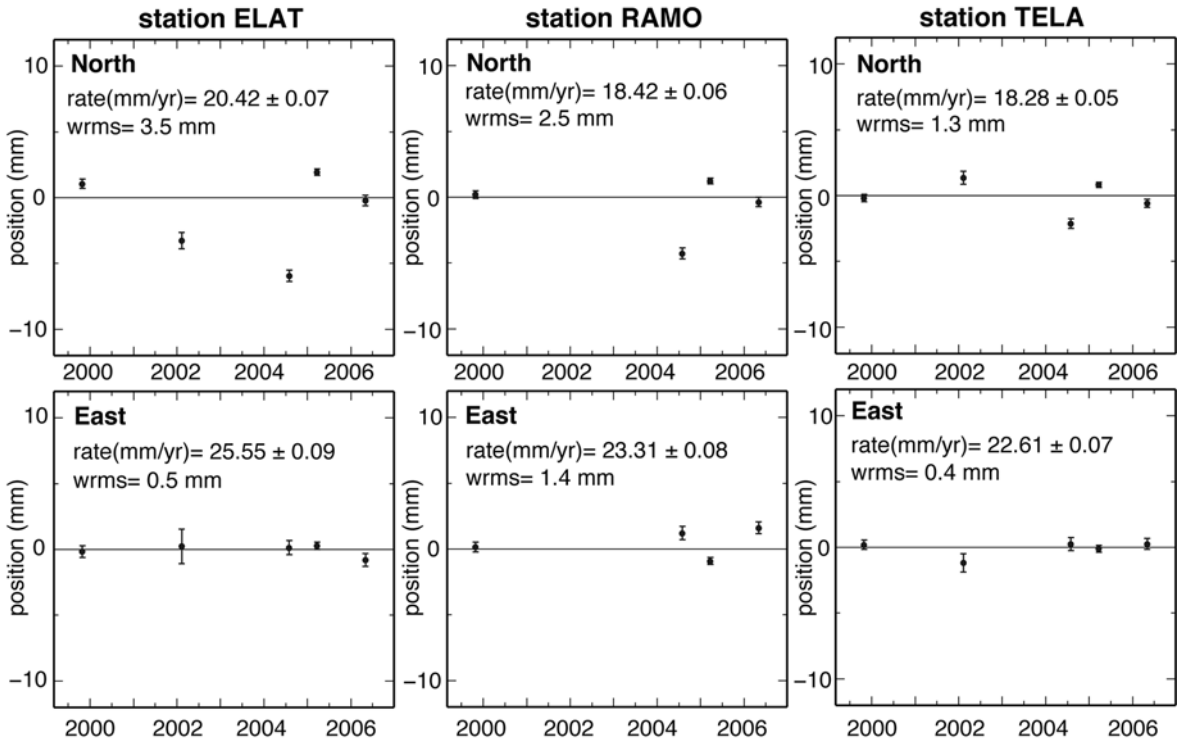

Figure 3. Long-term position time series for the Israeli sites ELAT, RAMO, and TELA in ITRF2000. The linear trend has been removed to appreciate the residues. Error bars represent 1-sigma formal uncertainties and thus underestimate the actual uncertainty. Except for the north component of ELAT in 2004, positions are well lined up. RAMO was not included in 2002 because of bad quality data (see http://sideshow.jpl.nasa.gov/mbh/all/RAMO.html).

Table 4. Euler Vectors Considered in This Study[a]

No.	Latitude (°N)	Longitude (°E)	Ω (deg/Ma)	$\sigma\omega$ (deg/Ma)	σ_{maj} or Δlong	σ_{min} or Δlat	Azimuth[b] (deg)	Type of Data	Reference[c]
				Arabia in ITRF2000					
16	52.53	349.36	0.479	0.015	3.21	0.67	80	geod	this study
17	52.59	344.26	0.461	0.011	2.98	0.42	81	geod	Vigny
18	51.47	2.89	0.521	0.024	3.1	0.7	70	geod	Sella
				Sinai in ITRF2000					
19	53.52	359.09	0.477	0.150	16.85	0.56	64	geod	this study
20	57.98	334.89	0.3588	0.1042	26.59	0.31	96.2	geod	Wdow
				Nubia in ITRF2000					
21	50.48	277.99	0.265	0.003	1.26	0.74	84	geod	Vigny
				Arabia-Sinai					
1	4.68	93.50	−0.049	0.089	261.74	8.99	56	geod	this study
2	14.08	79.62	−0.074	0.129	208.87	8.38	59	geod	Vigny (Ar) and this study (Si)
3	32.31	2.92	0.116	-	-	-	-	geod	Vigny (Ar) and Wdow (Si)
4	32.9	13.3	0.14	-	-	-	-	geod	this study (Ar) and Wdow (Si)
5	32.64	20.74	0.178	-	-	-	-	geod	McC (Eu-Ar) and Wdow (Si-Eu)[d]
6	32.8	28.4	0.370	0.027	3.7	3.4	-	geod + EM	Reil
7	27.70	18.78	0.057	0.176	77.41	10.31	70	geod	Sella (Ar) and this study (Si)
8	28.76	30.01	0.211	0.158	5.72	3.86	-	geod	Sella (Ar) and Wdow (Si)[d]
9	32.8	22.6	0.283	-	-	-	-	RSSR + TA	JG
				Sinai-Nubia					
10	30.47	31.93	0.355	0.177	7.48	1.06	85	geod	this study (Si) and Vigny (Nu)
11	31.04	26.34	0.203	0.154	8.35	1.64	82.5	geod	Wdow
12	30.17	29.99	0.199	-	-	-	-	geod	Wdow (Si) and Vigny (Nu)
13	9.7	350.4	0.030	0.021	0.04	44.1	-	geod + EM	Reil
14	30.3	28.1	0.093	-	-	-	-	RSSR+TA	JG
				Arabia-Nubia					
15	31.59	23.25	0.336	0.023	2.45	1.20	76	geod	this study (Ar) + Vigny (Nu)

[a]Uncertainties are 1σ confidence level. Conventionally, Ω positive means counterclockwise rotation. No., reference numbers refer to Figure 8 and text; geod, geodesy; EM, elastic block modeling; RSSR+TA, Red Sea spreading rates and transform azimuths.
[b]Azimuth of semimajor axis of error ellipse.
[c]JG, *Joffe and Garfunkel* [1987]; McC, *McClusky et al.* [2003]; Reil, *Reilinger et al.* [2006]; Sella, *Sella et al.* [2002]; Vigny, *Vigny et al.* [2006]; Wdow, *Wdowinski et al.* [2004].
[d]Published by *Wdowinski et al.* [2004].

al. [2002] (Table 4), as only three stations were available at that time: KATZ (Golan Heights, Israel), BAHR (Bahrain) and Satellite Laser Ranging station 7832 (Riyadh). Also, KATZ is located too close to the DST (Figure 5) to represent stable Arabia, and BAHR and station 7832 are located less than 500 km from each other, so that this pair defines a poor geometry to constrain the rigid rotation of the block. Implications of the different poles for the regional kinematics are discussed in section 5.

3.2. Horizontal Velocity Field

[13] To analyze the horizontal velocity field, the rotation of Arabia relative to ITRF2000 was removed from the data (Table 3). Station RAMO was then used as a fixed reference point by simply subtracting its velocity from all the velocity vectors (Figure 5). This configuration gives ways to study internal deformation within Israel and shows that at the scale of a few hundred kilometers no significant rotation of Sinai is detectable.

[14] The general pattern shows velocity vectors oriented roughly parallel to the fault with amplitude increasing eastward (Figure 5). Because RAMO is fixed, velocities west of the fault are small, in the range of uncertainties. Eastward, velocities increase up to ∼5 mm/a at JFR0, the farthest point to the east.

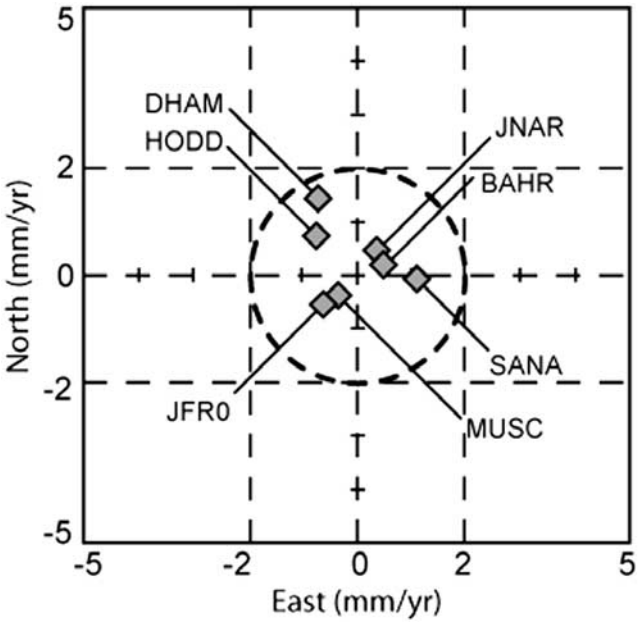

Figure 4. Residual velocities relative to Arabia for the sites used to determine the Arabia Euler vector in ITRF2000.

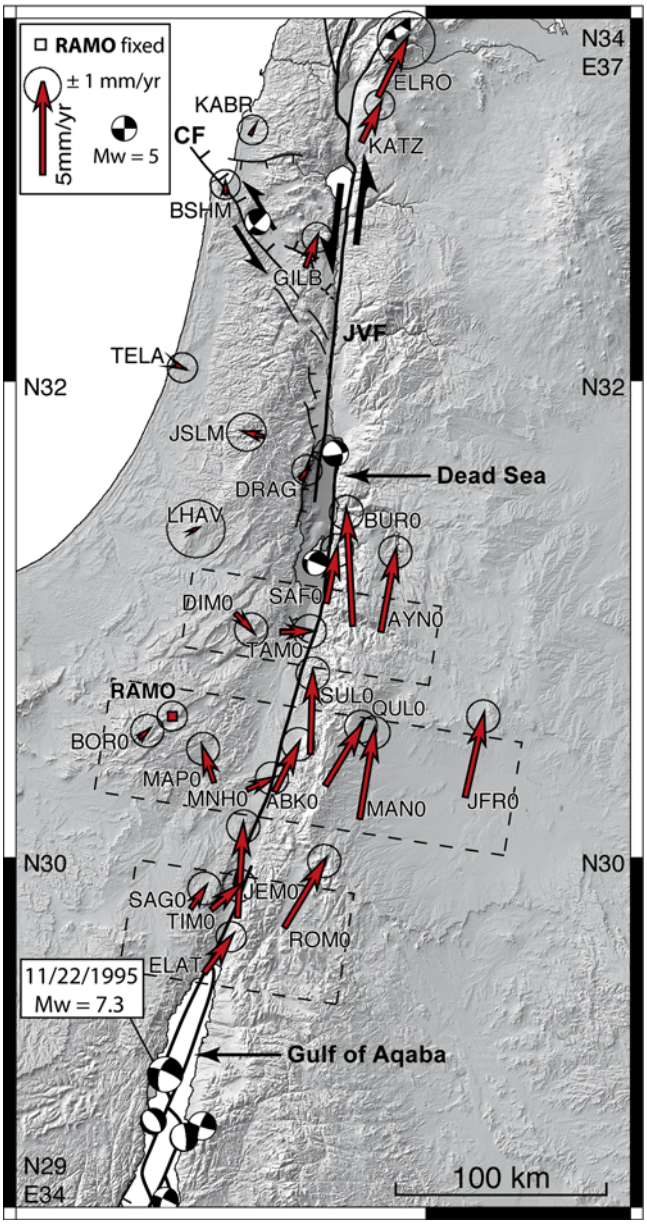

Figure 5. Tectonic map and horizontal velocity field plotted relative to site RAMO (rigid rotation of Arabia plate removed previously, see text). Error ellipses are 1-sigma, in agreement with Table 3. Campaign sites can be distinguished from their names ending by "0." Also shown focal mechanisms of events with $M_L > 5$ that occurred since 1976 (USGS (http://www.seismology.harvard.edu) and GII (http://www.gii.co.il) databases). Lines with tick marks are normal faults, lines with triangles are thrusts, and black arrows indicate strike-slip motion. CF, Carmel fault; LGEZ, Lower Galilee extension zone; JVF, Jordan Valley fault.

[15] Two vectors are not consistent with this pattern at BUR0 and JEM0. Site BUR0, located about 15 km from the fault, shows a slip that is higher than the easternmost site JFR0. Station BUR0 was measured 8 h only in 1999, which might be too short to get a reliable position and is statistically weak. In addition, the long-term stability of the BUR0 benchmark is questionable. Site JEM0 moves along the fault strike as fast as JFR0, while it is located only few kilometers from the fault. At this site, the benchmark was destroyed between the two campaigns, and it needed to be reinstalled. Although we suspect that the anomalous observations at BUR0 and JEM0 are due to data acquisition problems, we cannot rule out that it is related to transient deformation during the earthquake cycle or to creeping on the fault [e.g., *Bürgmann et al.*, 2000; *Pollitz*, 2001; *Johnson and Segall*, 2004]. This is discussed in more detail in section 3.4.

[16] In addition to the general strike-slip motion, sites ELAT, TIM0, MNH0, and TAM0, located west of the fault on the edge of the Araba Valley, show a small coherent component of slip of about 1.5 mm/a eastward. Although this pattern may not be significant compared to uncertainties (Figure 6e), we suggest that this deformation could be due to normal motion related to the faults bordering the valley [*Garfunkel*, 1981; *Kesten et al.*, 2007; *Hofstetter et al.*, 2007]. Note, however, that the fault-perpendicular components of the velocity field (Figure 6e) show that the displacement is limited to the near-fault field, not attesting to any plate divergence.

[17] North of the Dead Sea basin, we rely on Israeli permanent stations to survey the deformation. Sites located close to the Jordan Valley fault (GILB, KATZ) reflect elastic loading, as in the south. Other tectonic features in the area are the Carmel fault (CF) and the Lower Galilee extension zone, well expressed in the topography between sites BSHM and GILB and Lake Tiberias (Figure 5). Although data are sparse, our GPS observations do not show significant relative motion in this area, in agreement with *Wdowinski et al.* [2004] based on a similar data set. Normal and left-lateral motion is reported on CF from geomorphology and geological data [*DeSitter*, 1962; *Arad*, 1965; *Freund*, 1970; *Ron et al.*, 1984; *Ben-Gai and Ben-Avraham*, 1995; *Gluck*, 2002; *Matmon et al.*, 2003; *Rotstein et al.*, 2004], as well as fault plane solutions [*Hofstetter et al.*, 1996, 2007; *Salamon et al.*, 1996] (Figure 5), suggesting that it is still active today. According to geological observations [*DeSitter*, 1962; *Arad*, 1965; *Freund*, 1970] and timing of the deformation [*Matmon et al.*, 2003], left-lateral slip rate would be about 0.2–1.3 mm/a, which is indeed hardly detectable using GPS. It suggests that motion accommodated on CF is at most in the order of the error bars, namely, 1 mm/a.

3.3. Postseismic Deformation due to Past Earthquakes

[18] According to historical seismicity and paleoseismological investigations [e.g., *Abou Karaki*, 1987; *Ambraseys et al.*, 1994; *Amiran et al.*, 1994; *Guidoboni et al.*, 1994; *Klinger et al.*, 2000b; *Zilberman et al.*, 2005], the last magnitude > 7 earthquake occurred in the southern Araba Valley in A.D. 1068. Magnitude 6.5–7 events are reported also in A.D. 1212, A.D. 1293, and A.D. 1458 that could be tentatively located between the Gulf of Aqaba and the Dead Sea. All these events were identified as breccia layers in Dead Sea sediment cores [*Agnon et al.*, 2006], corroborating the historical evidence.

[19] Since the beginning of instrumental seismology, the Araba Valley experienced only one large earthquake, the M_w 7.3 earthquake in the Gulf of Aqaba (Figure 5). This event occurred on 22 November 1995, 4 years before our first

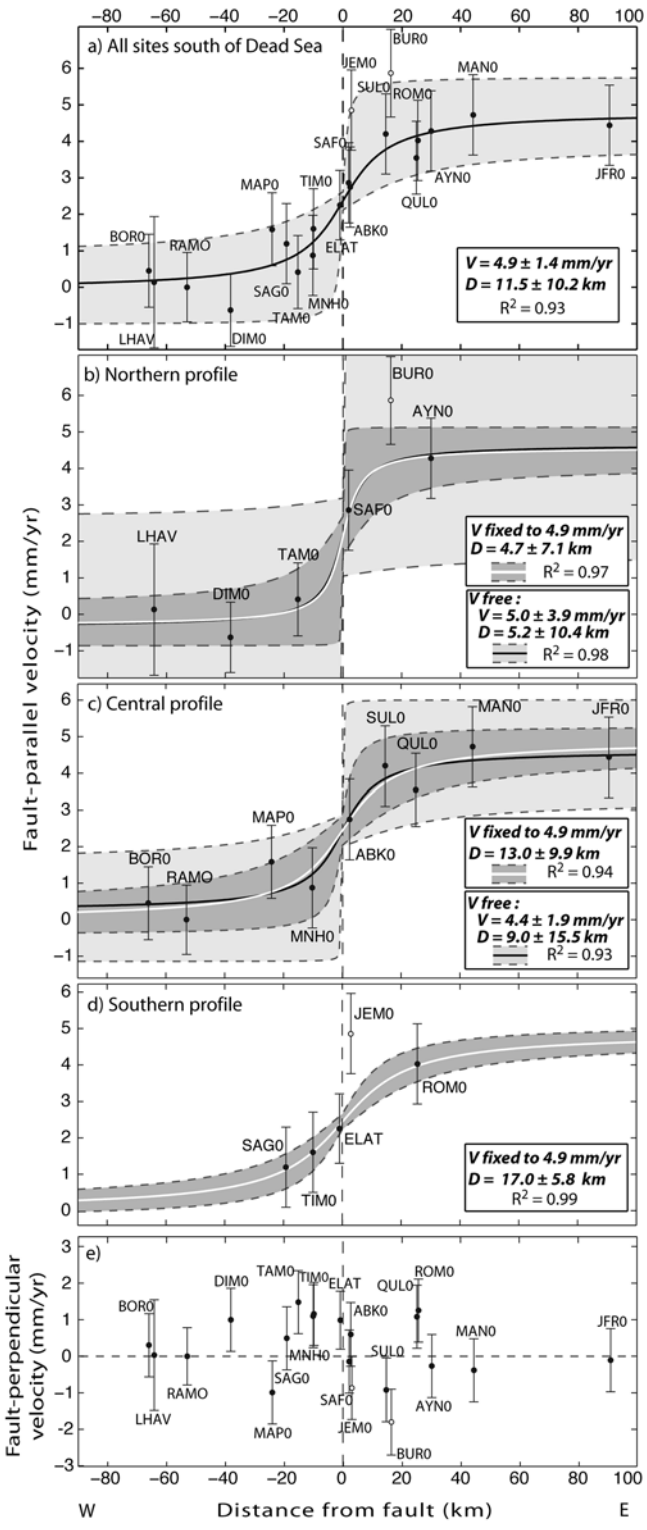

Figure 6. Observed fault-parallel velocities and best fit models. Error bars on observed velocities are 1-sigma confidence level. Continuous lines are best fit curves, and dashed lines define 95% confidence envelopes. The quality of the fit is indicated on each graph by the correlation coefficient R^2. V and D are best fit slip rate and locking depth, respectively; uncertainties are 95% confidence level. Open circles indicate sites not included in the computation (see text).

campaign (October 1999). Modeling of seismological data and interferometric synthetic aperture radar (InSAR) data [*Klinger et al.*, 1999, 2000c; *Baer et al.*, 1999; *Shamir et al.*, 2003] suggests that the rupture stopped about 25 to 40 km south of ELAT, the nearest station included in our study. No local GPS data from that time are available, but InSAR data covering the period of a week to 5 years after the earthquake show deformation very localized and restricted to fault steps along the Wadi Araba [*Sarti et al.*, 2003; *Finzi*, 2005]. It is not yet clear whether this deformation is related to the postseismic stage of the 1995 earthquake. Postseismic deformation studies for other M_w 7–7.5 strike-slip earthquakes have recognized that if some postseismic deformation can be identified, it is usually localized in the vicinity of the rupture (10 to 20 km of the main rupture) and limited in time from few months to about 3 years [*Peltzer et al.*, 1998; *Ergintav et al.*, 2002; *Jacobs et al.*, 2002; *Savage et al.*, 2003]. We therefore believe that our GPS data is not biased by any postseismic deformation due to former seismic activity along the southern segments of the DST, as supported by linear time series at sites ELAT and RAMO (Figure 3).

3.4. Slip Rate Estimates From Elastic Modeling of Fault-Parallel Velocities

[20] At first order, the observed velocity field (Figure 5) seems in good agreement with elastic loading on a locked dislocation that accommodates pure left-lateral shear at depth [e.g., *Savage and Burford*, 1973].

[21] Estimate of the slip rate was achieved by fitting our GPS data to a locked fault model consisting of an elastic seismogenic layer of thickness D (also called locking depth) overlying two blocks sliding horizontally relative to each other at velocity V along an infinitely long dislocation [*Savage and Burford*, 1973]. Equation (1) describes the theoretical velocity field observed at the surface, as a function of the distance x from the dislocation (i.e., the fault):

$$v(x) = a + \frac{V}{\pi}\arctan\left(\frac{x}{D}\right), \tag{1}$$

where the coefficient a defines the vertical origin of the curve. Parameter V controls the amplitude of the arctangent whereas its curvature is proportional to $1/D$. A nonlinear least squares procedure that does not take into account error bars on the data was used to derive parameters a, V, and D and their 2-sigma uncertainties. Weight has been applied inversely proportional to uncertainties for each data point, and sites JEM0 and BUR0 have been discarded from best fit computations (see discussion in section 3.2). North of the Dead Sea basin, the lack of stations located far from the fault to the east does not allow us to bring significant constraints on the slip rate. Our investigation is therefore limited only to the data acquired south of the Dead Sea. This limitation actually minimizes biases caused by fault geometrical complexities as the fault south of the Dead Sea is characterized by a single-strand linear geometry (Figure 5).

[22] Figure 6a shows fault-parallel velocities projected along azimuth N16, as a function of distance from the fault and the best fit curve with 95% confidence envelope, for all

sites south of the Dead Sea. The slip rate we derived from this data set is 4.9 ± 1.4 mm/a, well constrained by points located on both sides of the fault, as far as 70 km to the west and 90 km to the east. Best fit locking depth is 11.5 km with a large uncertainty of 10.2 km; this preferred value, however, is in agreement with previous results based on GPS profiles along the DST, in Israel [*Wdowinski et al.*, 2004] and in Lebanon [*Gomez et al.*, 2007]. It is also consistent with the observed nucleation depths of earthquakes for continental strike-slip faults [*Magistrale*, 2002], and especially those reported on the DST [*Aldersons et al.*, 2003; *Shamir et al.*, 2005; http://www.gii.co.il]. In our model the position of the dislocation is not free, but fixed to the location of the fault as observed in the field and from geophysics [e.g., *Garfunkel*, 1981; *ten Brink et al.*, 1999; *Haberland et al.*, 2003]. Match between the modeled dislocation and fault trace is supported by the high quality of the fit to the data.

[23] In the second step, individual fits were computed for each profile (Figures 6b, 6c, and 6d). As the data can be too sparse to sample far field motion, we also test an alternative fitting strategy, fixing V to the value previously found, to invert only for parameters a and locking depth D, in order to detect possible variations of D along the fault.

[24] For the northern profile, the far field is constrained only by LHAV for which the uncertainty is large. The three-parameter inversion provides a slip rate of 5.0 ± 3.9 mm/a (Figure 6b). Although uncertainty is large, consistency between the result derived only from this subset of data and the entire data set demonstrates the stability of the slip rate we obtained. Fixing V to the value derived from the full data set, the best fit locking depth is 4.7 ± 7.1 km. The deepest value within this 95% confidence interval, 11.8 km, is still not in agreement with seismological observations of *Aldersons et al.* [2003] in the Dead Sea basin area: for the period 1984–1997, 60% of microearthquakes occurred at depths of 20 to 32 km, suggesting a brittle rheology down to the lower crust. Some creep below ~10 km depth could reconcile these observations; however, we argue that distribution of the GPS sites does not constrain very well the curvature of the model near the fault.

[25] For the central profile, V free and V fixed inversion schemes were also tested (Figure 6c). In both cases the quality of the fit is good. Best fit locking depths are 9.0 ± 15.5 km and 13.0 ± 9.9 km, respectively, if V is kept free or fixed. In the latter case, best fit slip rate is 4.4 ± 1.9 mm/a, which is consistent with our first result of 4.9 ± 1.4 mm/a.

[26] For the southern profile (Figure 6d), no data is available to constrain the far field and V free inversion would be meaningless. If V is fixed, inversion yields a locking depth of 17.0 ± 4.9 km, which is consistent with the depth of 1995 Aqaba earthquake hypocenter (10–18 km [*Dziewonski et al.*, 1997; *Hofstetter et al.*, 2003]).

[27] As mentioned earlier, although we suspect our results at BUR0 and JEM0 to be due to acquisition problems, alternative explanations were tested. It is worth noting that for BUR0 and JEM0, if one considers uncertainties, they both fall in the 95% confidence envelope of our preferred model (Figure 6a) showing that they are still consistent with the model. In the case of BUR0, similar anomalous signal has been observed that was related to transient deformation following an earthquake as predicted by viscoelastic models [e.g., *Pollitz*, 2001; *Meade and Hager*, 2005]. However, as no large earthquake occurred on this fault segment recently, we find no justification in introducing such more elaborate models to explain the data at BUR0. In the case of JEM0, because it is closer to the Aqaba earthquake area and because some possible creep has been reported in this area [*Finzi*, 2005], we tried to introduce some creep component in our model. Adding to equation (1) a term that takes into account slip along the locked part of the dislocation, both with parameters a, V, and D free or kept fixed, remained unsuccessful to explain the observation at JEM0. Thus, the motion observed at JEM0 is most likely due to the benchmark reinstallation issue.

[28] In summary, elastic locked fault modeling of 17 fault-parallel velocities located south of the Dead Sea basin yields a well constrained slip rate of 4.9 ± 1.4 mm/a. Constraining the locking depth precisely has been harder to achieve, probably because the velocity gradient around the fault is too close to the error bars. Best fit locking depth is about 12 km, which is consistent with other dislocation models discussed in the literature [e.g., *McClusky et al.*, 2003; *Wdowinski et al.*, 2004; *Socquet et al.*, 2006; *Gomez et al.*, 2007] and with nucleation depth of earthquakes on the DST [*Aldersons et al.*, 2003; *Shamir et al.*, 2005] as well as on other continental strike-slip faults [*Magistrale*, 2002]. Uncertainty on D for individual profiles, however, makes any further discussion about possible variations of locking depth along strike quite speculative.

[29] Although one should keep in mind that most data used here to compute the velocity field and to derive the slip rate are based only on two GPS campaign measurements, the consistency between the 17 individual vectors is worth noting. Such internal consistency of data indicates the robustness of our result and is unlikely to be coincident. Further measurements that will, hopefully, provide tests to our interpretation should be carried out in the next years.

4. Discussion of the GPS Results With Previous Slip Rate Estimates

[30] Earlier attempts have been made to measure the present-day slip rate using GPS, along the southern part of the DST. However, the small number of permanent GPS stations in that region and the lack of data east of the DST were a major limitation. *Pe'eri et al.* [2002], using ~3 years of continuous data acquired by the first three stations of the GIL network, ELAT, TELA, and KATZ, yielded a preliminary slip rate of 2.6 ± 1.1 mm/a. Combining a set of 10 stations located south of Lebanon, *Wdowinski et al.* [2004] provided a slip rate of 3.7 ± 0.4 mm/a. Distinction between north and south of the Carmel fault led to 4.2 ± 1.1 mm/a and 2.9 ± 1.1 mm/a, respectively. Unfortunately, these two studies were unable to provide good constraint for the far field motion to the east of the DST as the easternmost station was KATZ, located only a few kilometers from the fault (Figure 5). Hence, it is likely that they only sample part of the total motion across the DST. The best constrained 1-sigma intervals of *Wdowinski et al.* [2004] (3.3–4.1 mm/a and 3.1–5.3 mm/a when considering the northern sites) are in agreement with the lower part of our 2-sigma interval of 3.5–6.3 mm/a.

[31] Several studies investigated the slip rate along the Wadi Araba and Jordan Valley faults for longer time scales. *Marco et al.* [2005] estimated a minimum slip rate of 3 mm/a during the last 5 ka from offset buried channels along the northern shore of Lake Tiberias. South of Dead Sea, offset alluvial terraces and alluvial fan provided minimum slip rates of 4.5 ± 1.5 mm/a since the Pleistocene [*Klinger et al.*, 2000a; *Niemi et al.*, 2001] and 5.25 ± 2.25 mm/a since the Pliocene [*Ginat et al.*, 1998]. Reconstruction of initial geometries for geologic formations of Early Pliocene to Late Miocene yielded slip rates in the range of 3 to 7 mm/a [*Freund et al.*, 1968, 1970; *Garfunkel*, 1981; *Garfunkel and Ben-Avraham*, 2001]. Recently, *Makovsky et al.* [2008] measured 2–4 mm/a slip rate from an offset Holocene coral terrace at the western strand of the Gulf of Aqaba, where additional slip is likely partitioned to the eastern gulf.

[32] Farther north, recent works have brought new estimates of the slip rate along the restraining bend in Lebanon and along the strike-slip segment in Syria. From geological observations in Lebanon, the total left-lateral motion across the Yammouneh fault and the Serghaya fault has been estimated at 6.5 ± 1.5 mm/a during the Holocene [*Gomez et al.*, 2003; *Daëron et al.*, 2004]. Ninety-kilometer-long baseline GPS data across the Lebanese range yielded a lower rate closer to 4.5 mm/a [*Gomez et al.*, 2007]. In addition to the strike-slip component, thrusting across the Lebanese range, estimated in the order of 1 to 3 mm/a [*Daëron et al.*, 2004; *Elias*, 2006; *Elias et al.*, 2007], should also be considered.

[33] Along the Missyaf fault in Syria, left-lateral offset accumulated by the last three earthquakes since 2 ka provided an average slip rate of 6.9 ± 0.1 mm/a [*Meghraoui et al.*, 2003]. This value is higher than most observations to the south and slightly higher than the slip in Lebanon. Following M. Meghraoui and colleagues, we argue that slip rate averaged during 2 ka is very dependent of the earthquake cycle that they determined to be about 830 years along Missyaf fault.

[34] From these different observations, it seems that the new GPS results for the DST south of Lebanon agree reasonably well with the geological observations at different time scales for the same area, converging to a slip rate in the order of 5 ± 2 mm/a. It is worth noting that this area has not been affected by any large earthquake since A.D. 1068. In the northern part of the DST, the situation is different and some discrepancy, although not too large, exists between the long-term and the present-day slip rates. In these regions, the fault has been activated by large earthquakes more recently [*Gomez et al.*, 2003; *Meghraoui et al.*, 2003; *Daëron et al.*, 2005, 2007; *Akyuz et al.*, 2006], which may affect short-term measurements and bring some difficulties in direct comparison between slip rates at different time scales [*Perfettini and Avouac*, 2004; *Chéry and Vernant*, 2006], especially in the Lebanese range where the fault system is complex with partitioning of motion between strike-slip and thrusting [*Tapponnier et al.*, 2001; *Elias*, 2006; *Elias et al.*, 2007].

[35] Because of the lack of data constraining the motion of the Sinai subplate until very recently, regional kinematic models usually ignored the Gulf of Suez and only considered the relative motion between Arabia and Nubia. As a direct consequence the motion along the DST has usually been overestimated by at least 1 mm/a [*Garfunkel and Bartov*, 1977; *Bosworth and Taviani*, 1996; *Mahmoud et al.*, 2005; *Riguzzi et al.*, 2006]. Typically, determination of slip rate based on the analyses of 45 spreading rates from the Red Sea since 3.2 Ma, but ignoring a component of opening across the Gulf of Suez, led to the value of 8.3 ± 2.9 mm/a on the southern DST since the Pliocene [*Chu and Gordon*, 1998], which barely overlaps values discussed above, based on direct measurements along the southern DST.

[36] To overcome this limitation, *Joffe and Garfunkel* [1987] included Sinai in a model that was mostly constrained by spreading rates from the central Red Sea and fault azimuths of DST south of Lebanon from *Garfunkel et al.* [1981]. They obtained a left-lateral slip rate of 6 mm/a along the southern DST and 1.5 mm/a of opening across the southern part of the Gulf of Suez. However, they predicted significantly lower opening across the northern Red Sea than the spreading rates published more recently by *Chu and Gordon* [1998] meaning that the predicted motion accommodated by the DST and the Gulf of Suez has probably been underestimated.

[37] The first global plate motion model based on geodetic data that includes the Arabia plate is REVEL [*Sella et al.*, 2002]. As discussed in section 3.1, rotation parameters in ITRF for Arabia plate were poorly constrained and the Arabia-Nubia Euler vector from REVEL predicted a rate of 4 mm/a along the DST, which is slightly lower than our direct measurement across the fault. Addition of recent GPS data at a regional scale, in Arabia peninsula, Sinai, Anatolia, Iran, and Africa has greatly improved the determination of the Euler vector for Arabia-Nubia. *McClusky et al.* [2003] and *Vigny et al.* [2006] predicted slip rate of 5.9 ± 2 mm/a and 7.4 ± 1 mm/a, respectively, along southern DST, ignoring Sinai. Recent models including the Gulf of Suez and the Sinai as a subplate led to a slip rate of 4.4 ± 0.3 mm/a along the southern DST [*Mahmoud et al.*, 2005; *Reilinger et al.*, 2006], in good agreement with our local measurement.

5. Arabia-Sinai-Nubia Relative Motion

[38] Besides the determination of the present-day slip rate along the southern section of the DST, the data presented here can also be used to further constrain relative motion between Arabia, Sinai, and Nubia. We derive Euler vectors of Arabia and Sinai in ITRF2000. Complemented by the most recent results published for Nubia, we compute all possible combinations of relative Euler vectors for the Arabia–Sinai pair and the Sinai–Nubia pair and we compare them with previous results. Relevance of the different Euler poles is discussed in the light of the slip rates predicted along the tectonic boundaries of Sinai, the DST, and the Gulf of Suez.

5.1. Rotation Parameters in ITRF2000

[39] Arabia plate rotation parameters have been determined and discussed in section 3.1 (Figure 4 and Table 4). In the following, we consider both Euler vectors determined in this study and by *Vigny et al.* [2006]. Although it is less constrained, we also take into account the result of *Sella et al.* [2002]. Having no new data for Nubia, we use Euler vectors previously published in the literature. Consistency

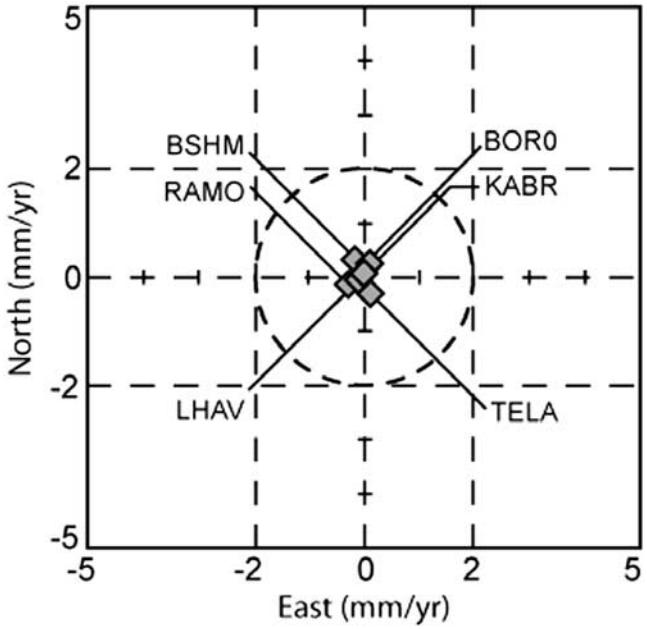

Figure 7. Residual velocities relative to Sinai for the sites used to determine the Sinai block Euler vector in ITRF2000.

between most recent solutions by *Vigny et al.* [2006] and *Fernandes et al.* [2003], despite the use of different data sets, indicates that the motion of Africa is quite well constrained today. In the following we choose to use the solution of *Vigny et al.* [2006].

[40] To determine the rotation parameters for the Sinai subplate, the only data available are located in Israel. Because of the vicinity of the DST, only sites BOR0, LHAV, RAMO, and TELA (Figure 5) can be considered to belong to stable Sinai. In section 3.2 we argue that the motion along the Carmel fault is negligible. Thus, we include sites BSHM and KABR in stable Sinai, and we minimize residues for this set of six stations (BOR0 and RAMO being very close to each other). We obtain the following Euler vector for Sinai subplate in ITRF2000: N53.52, E359.09 and $\Omega = 0.477 \pm 0.15°$/Ma (Table 4). Uncertainties associated to this result are quite high (for comparison, see Table 4), while misfit on each vector is very small (Figure 7), meaning that the movement of the block is well defined, while the determination of the rotation parameters remains inaccurate. This can be explained by the large distance between Sinai and its pole of rotation, the small size of the Sinai block and the ill-defined geometry of the GPS stations, aligned in a north-south direction, which leads to an observed velocity field in ITRF2000 that is almost uniform (similar north components and 2 mm/a increase of east components toward the south, Table 3).

[41] It is worth noting that despite the use of a comparable data set, our result differs significantly from the one of *Wdowinski et al.* [2004]. Although uncertainties are in the same range and angular velocities are within error bars, the poles of rotation hardly overlap. In Sinai, their velocities and the velocities presented here agree within 0.5 mm/a for most sites and at most 1 mm/a (RMS between both sets of results is 0.6 mm/a), which is less than the uncertainty related both to the measurements and to the realizations of the ITRF. Comparing to the results from SOPAC, the misfit of our velocity field and of the one of *Wdowinski et al.* [2004] is 0.5 and 0.4 mm/a, respectively. Because the sites are located very close to each other, the small differences in both velocity fields could explain such large variation in the Euler vectors. We see no strong argument to favor one pole rather than the other. We emphasize that this discrepancy rather highlights the inaccuracy of any determination of an Euler vector for Sinai in ITRF, first, due to the small size of the block and to its movement in ITRF (pole located at a large distance), as explained in the previous paragraph, and second, due to its sensitivity to slight differences (even smaller than the uncertainties) in the velocity field.

5.2. Relative Plate Motions

[42] Euler vectors of Arabia relative to Sinai and of Sinai relative to Nubia are reported in Table 4. They result from the combination of the Euler vectors in ITRF2000 discussed above. When possible, uncertainties have been calculated by adding variance-covariance matrices associated to determination of the two poles in ITRF2000.

5.2.1. Arabia-Sinai

[43] Combination of available poles of rotation in ITRF2000 for Arabia and Sinai leads to a large set of possible poles and their associated angular velocities, some of them characterized by large uncertainties (Table 4 and Figure 8). As discussed in the following, large amplitudes of uncertainties for the relative poles can be explained first by the trade-off between the pole position and the angular velocity and second by the subtraction of Euler vectors that are very similar in direction and length, including the ITRF2000 Sinai pole characterized by notably large error bars.

[44] We illustrate on Figure 8 the domain of possible positions for Euler poles of Arabia relative to Sinai and associated values of angular velocities, at the 95% and 99% confidence level consistent with our data. The domain has the shape of two bananas, elongated along the great circle that passes by the area of observed velocities, materialized by a black dotted line on Figure 8. Within the domains, the absolute value of angular velocity Ω decreases when the distance from the pole to the Arabia plate increases, illustrating poorly defined rotation of Arabia relative to Sinai, characterized by an important trade-off between the distance from the pole to the plate boundary and the angular velocity. This is largely due to slow rotation along a short, almost straight, plate boundary and the relatively small size of Arabia plate.

[45] The Ω-negative domain (clockwise rotation), however, is not consistent with the long-term morphology of southern DST, described by *Garfunkel et al.* [1981] as en echelon small circles with a curvature toward the west. This questions the relevance of half of the 2-sigma solution envelope proposed here, including the best fit solution. This discrepancy could be explained by a recent change in the relative motion between Arabia and Sinai, which can hardly be confirmed or invalidated by other observations. Almost all Arabia-Sinai rotation poles derived from solutions already published in the literature (Table 4 and Figure 8) lie within the domain of our solution, if not, very close.

[46] As mentioned above, varying uncertainties of the Arabia-Sinai Euler poles presented here (Figure 8 and

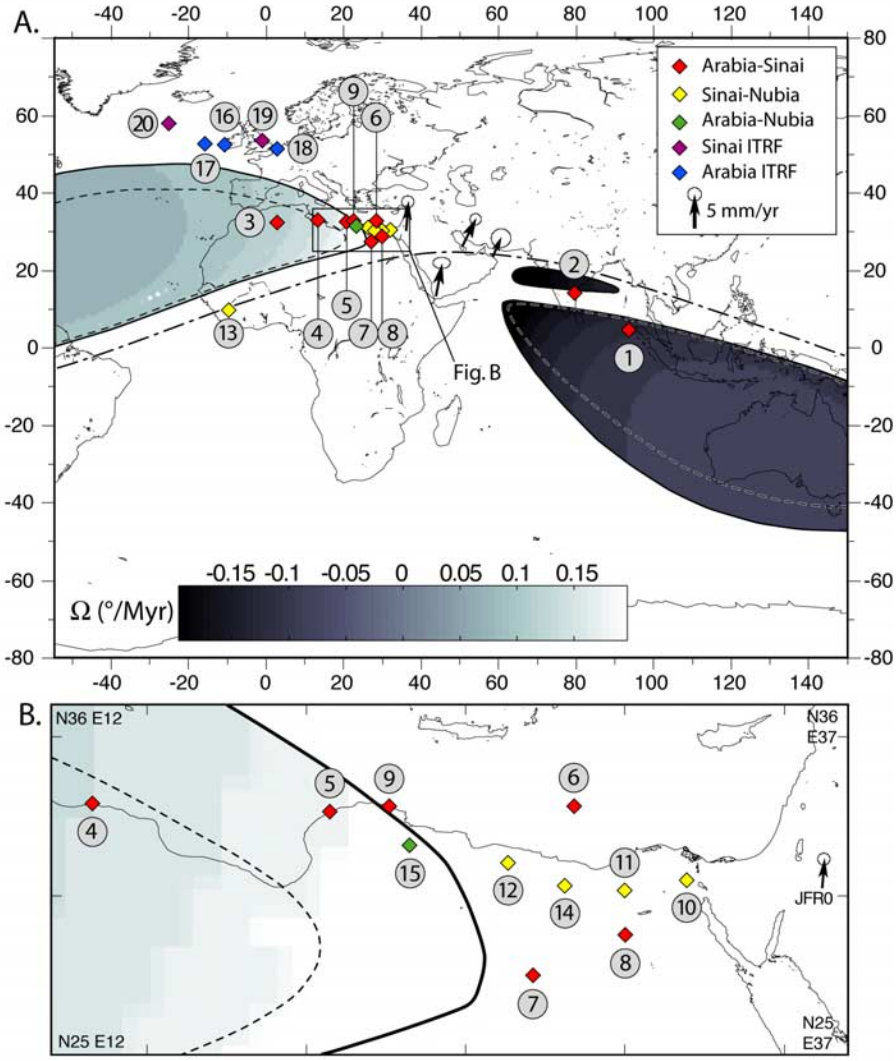

Figure 8. Possible domains for the location of the Euler pole of Arabia relative to Sinai from our study, at the 95% (dashed contour) and 99% (solid contour) confidence level. Because of symmetry effects on Earth, we explore only the half sphere centered on Arabia plate. Gray scale color bar represents the value of angular velocity Ω ($\Omega > 0$ for counterclockwise rotation). Other Arabia-Sinai poles are located and numbered as referenced in Table 4 (see Table 4 for value of Ω for these poles). Black arrows show Arabia velocity field relative to Sinai; only one vector is shown in Yemen (averaging the four stations). We also represent poles positions in ITRF2000 and for Sinai-Nubia and Arabia-Nubia relative motion (Table 4).

Table 4) is also related to subtraction of ITRF Euler vectors that have similar direction and length. This can be illustrated by the example of pole 1, affected by large uncertainties, and of pole 8 that has limited uncertainty. Pole 1 is obtained from poles 16 and 19 (Figure 8 and Table 4) that are located close to each other and which angular velocities are almost equal. By contrast, pole 8 involves poles 18 and 20, located farther from each other and which angular velocities differ significantly.

[47] For each combination, fault-perpendicular and fault-parallel components of slip are predicted along the different segments of the DST, from Wadi Araba fault to Missyaf fault in Syria (Table 5a). A selected set of predicted velocities is shown on Figure 9, together with vectors predicted by the Arabia-Nubia Euler pole neglecting the motion across the Gulf of Suez. In Lebanon, compression and left-lateral slip are calculated, considering the Yammouneh fault as the only active branch of DST. Slip in Lebanon and in Syria is overestimated by at most 1 mm/a because internal deformation of the Sinai plate at the Carmel fault and in the Lower Galilee extension zone (see section 3.2) and deformation of the Arabia plate in the Palmyrides folds [*Chaimov et al.*, 1990] are not considered.

[48] Most of the Arabia-Sinai relative Euler vectors predict reasonable slip along the DST on its entire length (Table 5a and Figure 9). Exceptions are vectors involving Arabia rotation parameters of *Sella et al.* [2002] (updated to ITRF2000) (poles 7 and 8 in Tables 4 and 5a) that predict 1 to 2 mm/a of left-lateral slip along the DST, which is significantly slower than the result of any other study (see section 4). This inconsistency suggests that these poles should be excluded and that more recent solutions for

Table 5a. Predicted Velocity on the Arabia-Sinai Plate Boundary[a]

No.	Reference[b]	Wadi Araba (N16E)				Jordan Valley (N5E)				Lebanon (N28E)				Missyaf (N2E)			
		V_{para}	dV_{para}	V_{ortho}	dV_{ortho}	V_{para}	dV_{para}	V_{ortho}	dV_{ortho}	V_{para}	dV_{para}	V_{ortho}	dV_{ortho}	V_{para}	dV_{para}	V_{ortho}	dV_{ortho}
1	this study	4.7	1.2	−0.3	0.9	4.7	1.2	0.8	0.9	4.6	1.1	−1.0	1.1	4.6	1.9	1.2	1.1
2	Vigny (Ar) + this study (Si)	5.7	1.2	−0.4	0.7	5.6	0.9	0.9	0.7	5.6	1.1	−1.3	1.0	5.5	1.9	1.5	1.0
3	Vigny (Ar) + Wdow (Si)	6.0	-	−0.4	-	5.9	-	0.4	-	5.5	-	−2.3	-	6.0	-	0.2	-
4	this study (Ar) + Wdow (Si)	5.0	-	−0.2	-	5.0	-	0.3	-	4.6	-	−2.2	-	5.1	-	-0.2	-
5	McC (Eu-Ar) + Wdow (Si-Eu)	4.3	-	−0.1	-	4.3	-	0.1	-	3.8	-	−2.2	-	4.5	-	-0.6	-
6	Reil	4.5	-	0.7	-	4.3	-	0.2	-	3.7	-	−2.8	-	4.7	-	-1.6	-
7	Sella (Ar) + this study (Si)	1.5	1.4	−0.6	2.4	1.6	1.2	−0.5	2.3	1.2	1.5	−1.3	2.5	1.7	1.7	-0.7	2.1
8	Sella (Ar) + Wdow (Si)	1.7	-	−1.1	-	1.9	-	−1.6	-	0.9	-	−2.9	-	2.2	-	-2.6	-
9	JG	6.0	-	0.0	-	6.0	-	0.1	-	5.3	-	−3.2	-	6.2	-	-1.0	-

[a]No., reference numbers refer to Figure 8. V_{para} and V_{ortho} are fault-parallel and fault-perpendicular velocity components, respectively. $V_{para} > 0$ means left-lateral slip; $V_{ortho} > 0$ means extension. Azimuth of the fault segments is indicated in parentheses. Locations of predicted slip rates are Wadi Araba fault, N30.28 E35.27 (site ABK0); Jordan Valley fault, N32.25 E35.57; Yammouneh fault, N34.09 E36.01; Missyaf fault, N35.05 E36.33.

[b]JG, *Joffe and Garfunkel* [1987]; McC, *McClusky et al.* [2003]; Reil, *Reilinger et al.* [2006]; Sella, *Sella et al.* [2002]; Vigny, *Vigny et al.* [2006]; Wdow, *Wdowinski et al.* [2004].

Arabia should be used instead of the one of *Sella et al.* [2002]. As discussed in section 3.1, their Euler vector for Arabia is based on a small data set with poor distribution on the plate. The other relative Euler vectors are valid as they predict pure left-lateral slip along the Wadi Araba fault that is in very good agreement with our direct measurements and with previous geomorphology-based slip rates [*Ginat et al.*, 1998; *Klinger et al.*, 2000a; *Niemi et al.*, 2001].

[49] In Lebanon, left-lateral slip is in agreement with GPS results from *Gomez et al.* [2007] and is within the lower half of the geological slip rates from *Daëron et al.* [2004] and *Gomez et al.* [2003]. The compressive component of the predicted motion is in the order of 1–3 mm/a estimate by *Elias* [2006], based on geological observations.

[50] North of Lebanon, predictions on Missyaf fault, even overestimated, are slower than the slip rate inferred by *Meghraoui et al.* [2003], that we suspect to be biased by the earthquake cycle. Along this segment, however, different Euler vectors predict interesting slight differences concerning the fault perpendicular velocity. Discarding results involving Arabia of *Sella et al.* [2002], some poles predict ~1 mm/a extension and others predict ~1 mm/a compression (Table 5a and Figure 9). The morphology of the fault in Syria (straight fault and wide pull-apart basin) shows that strike slip is dominant and that extension is more likely to occur than compression.

[51] We emphasize that even if the motion across the Gulf of Suez is small, Arabia-Sinai relative Euler vectors describe the kinematics along the DST much better than the Arabia-Nubia poles, which overestimate strike-slip along the DST and involve significant fault-perpendicular compression in Syria [e.g., *McClusky et al.*, 2003] (Figure 9), which one could not recognize in the geomorphology. Hence, geodetic observations provide clear confirmation for the existence of a Sinai subplate.

[52] To summarize, our compilation of newly computed and previously published Arabia-Sinai Euler vectors show a large variety of positions for poles and of angular velocities, the uncertainty associated to some of these poles being large. To ensure the relevance of all poles, we calculated the slip rate that they predict on the DST. This allowed us to reject the solutions involving the Euler vector of *Sella et al.* [2002] for the Arabia plate in ITRF. All the other poles, however, are valid. We do not favor any specific solution. Rather we point out that the possibility of so many different, but relevant, poles can be explained by the geometry of the plate boundary, which is a relatively short and straight transform fault, accommodating slow relative movement between the two blocks. In addition, the relative Euler vectors discussed here involve the rigid rotation of the Sinai block that is very inaccurate itself. Eventually, this leads to an important trade-off between the angular velocity and the distance from the pole to the Arabian plate.

5.2.2. Sinai-Nubia

[53] Following the same procedure as above we compute the different possible Euler vectors for the motion of Sinai relative to Nubia. At four locations along the Gulf of Suez we calculate velocity predicted by each pole, along strike and perpendicular to the orientation of the gulf and also perpendicular to en echelon right-lateral faults suggested by *Courtillot et al.* [1987] (Table 5b and Figure 9). Sinai-Nubia relative Euler vectors involving our result, the one of *Wdowinski et al.* [2004] and the one of *Vigny et al.* [2006] (poles 10, 11, and 12 in Table 4) show a general agreement on pole location in northern Egypt (Figure 8). They predict 1 to 2.5 mm/a of extension at the southern tip of the gulf, decreasing to the NW, associated with a slight left-lateral component (0–1 mm/a). When considering the right-lateral faults suggested by *Courtillot et al.* [1987], only the pole 10 predicts slight right-lateral slip. Given the uncertainty, the sense of fault-parallel motion could be slightly left-lateral as well as right-lateral. By contrast, the pole of *Reilinger et al.* [2006] is located significantly more to the southwest, in Guinea, and the angular velocity is much smaller (Table 4 and Figure 8). Their solution predicts left-lateral slip of ~2 mm/a and extension of <1 mm/a (Table 5b and Figure 9), which are, however, not significantly different from the other results, given the error bars.

[54] A direct geometric calculation can be made to constrain the kinematics of the Gulf of Suez, without incorporating indirect data derived from the ITRF2000 Sinai pole, by subtracting the slip along the DST according to this study from the Arabia-Nubia relative motion. We consider Arabia-Nubia Euler vector determined from this study and from *Vigny et al.* [2006] (N31.59, E23.25, Ω = 0.336°/Ma). The residual motion accommodated across the Gulf of Suez is then 1.6 mm/a of right-lateral slip and 1 mm/a of extension at the southern tip of the gulf. This result is intermediate between the solution of *Reilinger et al.* [2006] and the other solutions.

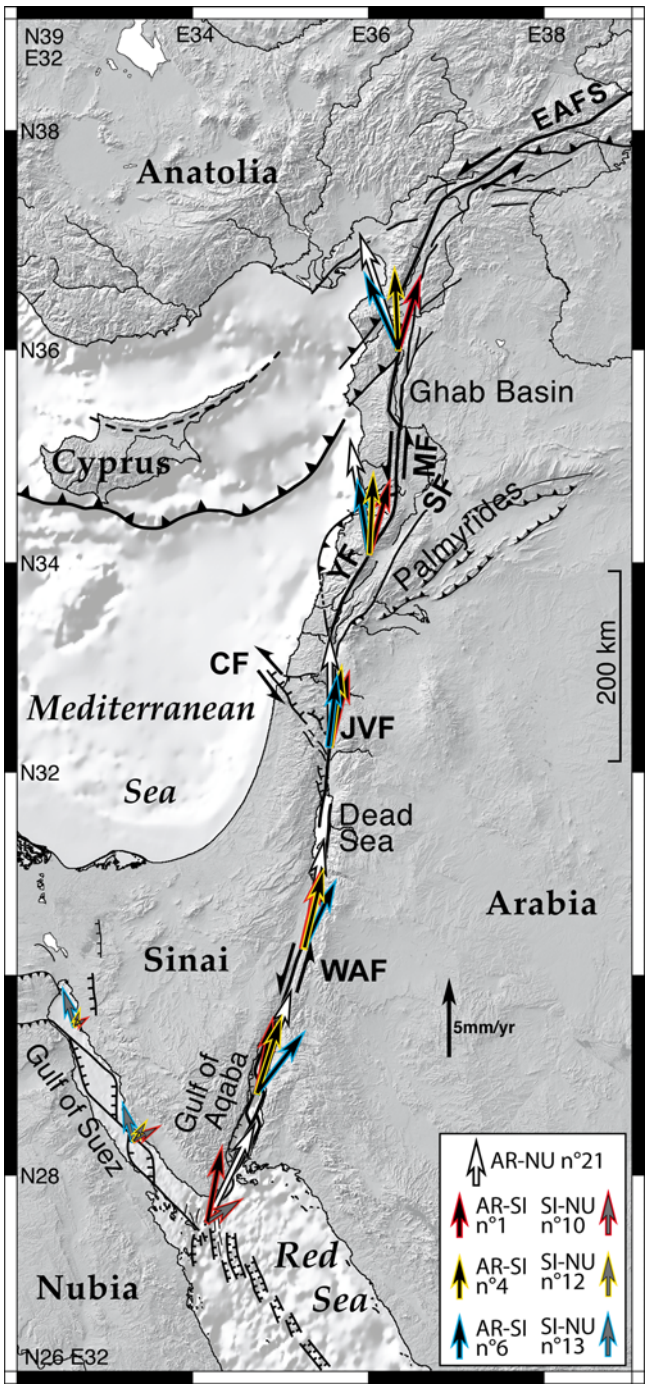

Figure 9. Regional kinematics predicted by selected Euler vectors. AR, Arabia; NU, Nubia; SI, Sinai. Pole numbers refer to Tables 4, 5a, and 5b. EAFS, East Anatolian fault system; WAF, Wadi Araba fault; JVF, Jordan Valley fault; CF, Carmel fault; YF, Yammouneh fault; SF, Serghaya fault; MF, Missyaf fault.

[55] A few studies attempted to quantify the motion across the Gulf of Suez. Opening is estimated to be ~1 mm/a at the southern tip of the gulf [*Garfunkel and Bartov*, 1977; *Bosworth and Taviani*, 1996]. Left-lateral component is reported from fault plane solutions [*Courtillot et al.*, 1987; *Salamon et al.*, 2003], and its amplitude has been tentatively estimated only by *Rybakov et al.* [1997] on the basis of a possible 80 km offset of a crustal magnetic anomaly observed in the basement. In contrast, *Tapponnier and Armijo* [1985] argue for right-lateral motion based on probably still active E-W thrusts and folds branching at the northwestern tip of the gulf and N-S normal fault in western Sinai (features mapped on Figure 9). Recent GPS studies [*Mahmoud et al.*, 2005; *Reilinger et al.*, 2006; *Riguzzi et al.*, 2006], although on the basis of a similar data set, do not agree with this interpretation. Both *Mahmoud et al.* [2005] and *Reilinger et al.* [2006] adjust local and regional data with an elastic block model and obtain 1–1.5 mm/a of extension and 2 mm/a of left-lateral slip. *Riguzzi et al.* [2006] instead suggest a compressive stress field that they interpret as postseismic relaxation related to 1995 Gulf of Aqaba earthquake (see section 3.3), its aftershocks and a few other earthquakes of magnitude 4 to 6 that occurred in the Gulf of Aqaba and in the Gulf of Suez. These differences in interpretation might be partly due to the fact that the velocities that they determine are in the order of the error ellipses (~1 mm/a). As mentioned by *Mahmoud et al.* [2005], the motion that they obtain across the Gulf of Suez is essentially controlled by data located on stable Sinai and Nubia. Velocities derived from all the Sinai-Nubia Euler vectors are in good agreement with geological and GPS observations but do not contribute to resolving the sense of lateral movement across the Gulf of Suez.

5.2.3. Arabia-Nubia

[56] From the new data set we have presented here, we could not directly measure the relative motion between Arabia and Nubia. We could, however, determine the Euler vector of Arabia in ITRF2000 and combine it with existing poles for Nubia, determined by other studies, to see how it compares when looking at the relative motion between Arabia and Nubia. Following *Calais et al.* [2003], *Vigny et al.* [2006] have proposed a slow down of the Arabia plate relative to Nubia, Somalia, and Eurasia, on the basis of a 15–20% decrease of velocities predicted by their model compared to velocities since 3.2 Ma from models such as NUVEL-1A [*DeMets et al.*, 1990, 1994] and the study of *Chu and Gordon* [1998]. As mentioned by *Vigny et al.* [2006], such a decrease remains tenuous, being in the order, or slightly higher, than the error bars. We argue that Arabia Euler vector in ITRF2000 determined in this study is an improvement compared to the solution proposed by *Vigny et al.* [2006], due to better data geometry. When this new pole is combined with their poles for Nubia, Somalia and Eurasia, predicted velocities show high consistency with their results, reinforcing the assumption that relative velocity of Arabia has been slowing down recently.

6. Conclusions

[57] On the basis of new campaign GPS data in Israel and Jordan, we image the present-day deformation across the southern segment of the Dead Sea Transform, the Wadi Araba fault. The horizontal velocity field relative to stable Arabia is well determined and shows pure left-lateral motion on the fault. Elastic locked fault modeling of 17 fault-parallel velocities distributed along profiles perpendicular to the fault provides a best fit slip rate of 4.9 ±

Table 5b. Predicted Velocity on the Sinai-Nubia Plate Boundary[a]

No.	Reference	Velocity Calculation Method[b]	N27.96 E33.88				N28.45 E33.50				N29.00 E33.23				N29.50 E32.75			
			V_{para}	dV_{para}	V_{ortho}	dV_{ortho}	V_{para}	dV_{para}	V_{ortho}	dV_{ortho}	V_{para}	dV_{para}	V_{ortho}	dV_{ortho}	V_{para}	dV_{para}	V_{ortho}	dV_{ortho}
10	this study (Si) + Vigny (Nu)	1	0.0	1.9	2.1	0.8	0.0	1.9	1.7	0.6	0.1	1.7	1.3	0.6	0.0	1.6	0.8	0.6
		2	−0.6	1.9	2.0	0.8	−0.5	1.9	1.7	0.6	−0.3	1.7	1.2	0.6	-0.2	1.6	0.8	0.6
11	Wdow	1	1.4	-	2.5	-	1.4	-	2.3	-	1.4	-	2.0	-	1.4	-	1.8	-
		2	1.1	-	2.8	-	1.2	-	2.6	-	1.3	-	2.3	-	1.3	-	2.1	-
12	Wdow (Si) + Vigny (Nu)	1	0.6	-	1.4	-	0.6	-	1.2	-	0.6	-	1.0	-	0.6	-	0.7	-
		2	0.2	-	1.6	-	0.2	-	1.3	-	0.3	-	1.1	-	0.4	-	0.9	-
13	Reil	1	2.2	-	0.8	-	2.2	-	0.7	-	2.2	-	0.7	-	2.2	-	0.7	-
		2	1.9	-	1.3	-	1.9	-	1.3	-	2.0	-	1.3	-	2.0	-	1.2	-
14	JG	1	0.5	-	0.9	-	0.5	-	0.8	-	0.5	-	0.7	-	0.5	-	0.5	-
		2	0.2	-	1.0	-	0.3	-	0.9	-	0.3	-	0.8	-	0.3	-	0.7	-

[a]Same as Table 5a.
[b]Velocities have been calculated (1) along and perpendicular to the strike of the gulf, N34W and (2) on the right-lateral faults proposed by *Courtillot et al.* [1987], azimuth N50W.

1.4 mm/a, well constrained by far field sites located up to 70 km west of the fault and 90 km east of it. The best fit locking depth is about 12 km, which is consistent with nucleation depth of earthquakes on continental strike-slip faults [*Magistrale*, 2002] and with other dislocation models on the DST and other strike-slip faults [e.g., *Wdowinski et al.*, 2004; *Socquet et al.*, 2006; *Gomez et al.*, 2007]. Despite the fact that most of the fault-parallel velocities presented here are based only on two campaigns and are thus very sensitive to measurements issues, the consistency between the 17 independent vectors and their close agreement with the velocity field predicted by a locked fault model gives us confidence in our measurements and their final interpretation. Further measurements in the future would, however, usefully complement this data set.

[58] Several recent studies based on geodesy converge to a value around 5 mm/a of left-lateral slip on the southern part of the DST and in Lebanon, also in agreement with slip rates derived from geological observations, averaging longer periods of time. The slight discrepancy between geodetic and time-averaged rates that is observed in Lebanon and Syria might account for local modulation of the deformation by the seismic cycle.

[59] We also used our data, complemented by previous work of *Vigny et al.* [2006], to study the regional kinematics of Arabia, Nubia, and Sinai. We provide a new Euler vector for Arabia plate in ITRF2000 reference frame (N52.53, E349.36, Ω = 0.479°/Ma) based on a better data distribution. This result is in agreement with the idea of a slowdown of the collision of Arabia and Nubia into Eurasia suggested by *Calais et al.* [2003] and *Vigny et al.* [2006].

[60] We provide a new Euler vector of the Sinai subplate in ITRF2000 and relative Arabia-Sinai and Sinai-Nubia Euler vectors. We discuss the difficulties of the determination of such poles, because of the small size of Arabia and Sinai, the slow motion across the Gulf of Suez and the large trade-off between the location of Arabia-Sinai pole and its angular velocity. Even with an optimized distribution of data on the Sinai block, it might still be difficult to achieve a better picture of the regional kinematics. However, in spite of large uncertainties, Arabia-Sinai relative motion describes the kinematics along the DST better than Arabia-Nubia Euler vectors, supporting the existence of a Sinai subplate.

[61] Reconstruction of relative plate motions is useful for improved estimation of the deformation at the plate boundaries. Present-day motion on the DST is surveyed directly by GPS networks in Israel and Jordan and in Lebanon. On the northern DST, intraplate deformation prevents from determining the slip rate accurately on the basis of relative Euler vector alone. In addition, one could argue whether the Levant coast north of Lebanon, squeezed between the Mount Lebanon Thrust and the junction of the East Anatolian fault system with the Cyprian Arc (Figure 1), behaves as part of stable Sinai. Direct measurement from GPS profiles set up in ITRF2000 would resolve this question and the slip rate issue. Possible improvements of slip rate estimates across the Gulf of Suez would possibly include continuous GPS monitoring. Accurate knowledge of deformation taken at the DST and Gulf of Suez from direct measurement could then help better determination of the motion of Sinai relative to the surrounding plates and further study of the western extent of the Sinai subplate.

[62] **Acknowledgments.** We gratefully thank students, technicians, engineers, and researchers from Jordan, Israel, and France involved in the acquisition of the GPS data in 1999 and 2005, especially Y. Shaked, E. Kagan, O. Dor, R. Knafo, and people at the Survey of Israel (MAPI), the Geological Survey of Israel (GSI), and the Natural Resources Authority of Jordan (NRA). M. Golan has ingeniously eased the logistics in Israel. Special thanks are addressed to C. Vigny, A. Socquet, and C. Lasserre for fruitful discussion during this work. Thoughtful reviews by S. Wdowinski and F. Gomez have helped improve this manuscript. Financial support was provided by the French INSU/CNRS programs DyETI and ACI-FNS "Aleas et changements globaux," the French Embassy in Jordan and the French-Israeli Scientific and Technological Cooperation Joint Projects "Arc-en-ciel-Keshet." This is IPGP contribution 2399.

References

Abou Karaki, N. (1987), Synthèse et carte sismotectonique des pays de la bordure orientale de la Méditerranée: Sismicité du système de failles Jourdain-Mer Morte, Ph.D. thesis, Univ. de Strasbourg, Strasbourg, France.

Agnon, A., C. Migowski, and S. Marco (2006), Intraclast breccias in laminated sequences reviewed: Recorders of paleo-earthquakes, in *New Frontiers in Dead Sea Paleoenvironmental Research*, edited by Y. Enzel et al., *Spec. Pap. Geol. Soc. Am.*, *401*, 195–214, doi:10.1130/2006.2401(1113).

Akyuz, H. S., E. Altunel, V. Karabacak, and C. C. Yalciner (2006), Historical earthquake activity of the northern part of the Dead Sea Fault Zone,

southern Turkey, *Tectonophysics*, *426*, 281–293, doi:10.1016/j.tecto.2006.08.005.

Aldersons, F., Z. Ben-Avraham, A. Hofstetter, E. Kissling, and T. Al-Yazjeen (2003), Lower-crustal strength under the Dead Sea basin from local earthquake data and rheological modeling, *Earth Planet. Sci. Lett.*, *214*, 129–142, doi:10.1016/S0012-821X(03)00381-9.

Altamimi, Z., P. Sillard, and C. Boucher (2002), ITRF2000: A new release of the International Terrestrial Reference Frame for earth science applications, *J. Geophys. Res.*, *107*(B10), 2214, doi:10.1029/2001JB000561.

Ambraseys, N. N., C. P. Melville, and R. D. Adams (1994), *The Seismicity of Egypt, Arabia and the Red Sea: A Historical Review*, Cambridge Univ. Press, Cambridge, U.K.

Amiran, D. H. K., E. Arieh, and T. Turcotte (1994), Earthquakes in Israel and adjacent areas: Macroseismic observations since 100 BCE, *Isr. Explor. J.*, *44*, 260–305.

Arad, A. (1965), Geological outline of the Ramot-Menashe region (northern Israel), *Isr. J. Earth Sci.*, *14*, 18–32.

Baer, G., D. Sandwell, S. Williams, Y. Bock, and G. Shamir (1999), Coseismic deformation associated with the November 1995, M_w = 7.1 Nuweiba earthquake, Gulf of Elat (Aqaba), detected by synthetic aperture radar interferometry, *J. Geophys. Res.*, *104*(B11), 25,221–225,232, doi:10.1029/1999JB900216.

Ben-Gai, Y., and Z. Ben-Avraham (1995), Tectonic processes in offshore northern Israel and the evolution of the Carmel structure, *Mar. Pet. Geol.*, *12*, 533–548, doi:10.1016/0264-8172(95)91507-L.

Berberian, M., and G. C. P. King (1981), Towards a paleogeography and tectonic evolution of Iran, *Can. J. Earth Sci.*, *18*, 210–265.

Beutler, G., J. Kouba, and T. Springer (1993), Combining the orbits of the IGS processing centers, in *Proceedings of IGS Analysis Center Workshop*, edited by J. Kouba, pp. 20–56, Geod. Surv. Div., Nat. Resour. Can., Ottawa.

Bosworth, W., and M. Taviani (1996), Late quaternary reorientation of stress field and extension direction in the southern Gulf of Suez, Egypt: Evidence from uplifted coral terraces, mesoscopic fault arrays, and borehole breakouts, *Tectonics*, *15*, 791–802, doi:10.1029/95TC03851.

Bürgmann, R., D. Schmidt, R. M. Nadeau, M. d'Alessio, E. Fielding, D. Manaker, T. V. McEvilly, and M. H. Murray (2000), Earthquake potential along the northern Hayward fault, California, *Science*, *289*, 1178–1182, doi:10.1126/science.289.5482.1178.

Byrne, D. E., L. R. Sykes, and D. M. Davis (1992), Great thrust earthquakes and aseismic slip along the plate boundary of the Makran subduction zone, *J. Geophys. Res.*, *97*, 449–478, doi:10.1029/91JB02165.

Calais, E., C. DeMets, and J.-M. Nocquet (2003), Evidence for a post-3.16-Ma change in Nubia-Eurasia-North America plate motions?, *Earth Planet. Sci. Lett.*, *216*, 81–92, doi:10.1016/S0012-821X(03)00482-5.

Chaimov, T. A., M. Barazangi, D. Al-Saad, T. Sawaf, and A. Gebran (1990), Crustal shortening in the Palmyride fold belt, Syria, and implications for movement along the Dead Sea Fault System, *Tectonics*, *9*, 1369–1386, doi:10.1029/TC009i006p01369.

Chéry, J., and P. Vernant (2006), Lithospheric elasticity promotes episodic fault activity, *Earth Planet. Sci. Lett.*, *243*, 211–217, doi:10.1016/j.epsl.2005.12.014.

Chu, D., and R. Gordon (1998), Current plate motions across the Red Sea, *Geophys. J. Int.*, *135*, 313–328, doi:10.1046/j.1365-246X.1998.00658.x.

Courtillot, V., R. Armijo, and P. Tapponnier (1987), The Sinai triple junction revisited, *Tectonophysics*, *141*, 181–190, doi:10.1016/0040-1951(87)90184-3.

Daëron, M., L. Benedetti, P. Tapponnier, A. Sursock, and R. Finkel (2004), Constraints on the post (25-ka slip rate of the Yammouneh fault (Lebanon) using in-situ cosmogenic Cl^{36} dating of offset limestone-clast fans, *Earth Planet. Sci. Lett.*, *227*, 105–119, doi:10.1016/j.epsl.2004.07.014.

Daëron, M., Y. Klinger, P. Tapponnier, A. Elias, E. Jacques, and A. Sursock (2005), Sources of the large AD1202 and 1759 Near East earthquakes, *Geology*, *33*, 529–532, doi:10.1130/G21352.1.

Daëron, M., Y. Klinger, P. Tapponnier, A. Elias, E. Jacques, and A. Sursock (2007), 12,000-year-long record of 10 to 13 paleoearthquakes on the Yammoûneh fault, Levant fault system, Lebanon, *Bull. Seismol. Soc. Am.*, *97*, 749–771, doi:10.1785/0120060106.

DeMets, C., R. Gordon, D. Argus, and S. Stein (1990), Current plate motions, *Geophys. J. Int.*, *101*, 425–478, doi:10.1111/j.1365-246X.1990.tb06579.x.

DeMets, C., R. Gordon, D. Argus, and S. Stein (1994), Effects of recent revisions to the geomagnetic reversal time-scale on estimates of current plate motions, *Geophys. Res. Lett.*, *21*, 2191–2194, doi:10.1029/94GL02118.

DeSitter, L. U. (1962), Structural development of the Arabian shield in Palestine, *Geol. Mijnbouw*, *41*, 116–124.

Dziewonski, A. M., G. Ekstrom, and M. P. Salganik (1997), Centroid-moment tensor solution for October-December 1995, *Phys. Earth Planet. Inter.*, *101*, 1–12, doi:10.1016/S0031-9201(96)03199-8.

Elias, A. (2006), Le chevauchement de Tripoli-Saıuml;da: Croissance du Mont Liban et risque sismique, Ph.D. thesis, Inst. de Phys. du Globe de Paris, Paris.

Elias, A., P. Tapponnier, S. C. Singh, G. C. P. King, A. Briais, M. Daëron, H. Carton, A. Sursock, E. Jacques, R. Jomaa, and Y. Klinger (2007), Active thrusting offshore Mount Lebanon: Source of the tsunamigenic A.D. 551 Beirut-Tripoli earthquake, *Geology*, *35*, 755–758, doi:710.1130/G2363A.

Ellenblum, R., S. Marco, A. Agnon, T. Rockwell, and A. Boas (1998), Crusader castle torn apart by earthquake at dawn, 20 May 1202, *Geology*, *26*, 303–306, doi:10.1130/0091-7613(1998)026<0303:CCTABE>2.3.-CO;2.

Ergintav, S., R. Bürgmann, S. McClusky, R. Çakmak, R. E. Reilinger, O. Lenk, A. Barka, and H. Özener (2002), Postseismic deformation near the Zmit earthquake (17 August 1999, M 7.5) rupture zone, *Bull. Seismol. Soc. Am.*, *92*, 194–207, doi:10.1785/0120000836.

Feigl, K. L., et al. (1993), Space geodetic measurement of crustal deformation in central and southern California, 1984–1992, *J. Geophys. Res.*, *98*, 21,677–21,712, doi:10.1029/93JB02405.

Fernandes, R. M. S., B. A. C. Ambrosius, R. Noomen, L. Bastos, M. J. R. Wortel, W. Spakman, and R. Govers (2003), The relative motion between Africa and Eurasia as derived from ITRF2000 and GPS data, *Geophys. Res. Lett.*, *30*(16), 1828, doi:10.1029/2003GL017089.

Finzi, Y. (2005), Current deformation in the southern Dead Sea Transform: Radar interferometry measurements and their tectonic implications, *Rep. GSI/24/04*, Geol. Surv. of Isr., Jerusalem.

Freund, R. (1970), The geometry of faulting in Galilee, *Isr. J. Earth Sci.*, *19*, 189–205.

Freund, R., I. Zak, and Z. Garfunkel (1968), Age and rate of the sinistral movement along the Dead Sea Rift, *Nature*, *220*, 253–255, doi:10.1038/220253a0.

Freund, R., Z. Garfunkel, I. Zak, M. Goldberg, T. Weisbrod, and B. Derin (1970), The shear along the Dead Sea rift, *Philos. Trans. R. Soc. London, Ser. A*, *267*, 107–130, doi:10.1098/rsta.1970.0027.

Garfunkel, Z. (1981), Internal Structure of the Dead Sea leaky transform (Rift) in relation to plate kinematics, *Tectonophysics*, *80*, 81–108, doi:10.1016/0040-1951(81)90143-8.

Garfunkel, Z., and Y. Bartov (1977), The tectonics of the Suez Rift, *Bull. Geol. Surv. Isr.*, *71*, 1–44.

Garfunkel, Z., and Z. Ben-Avraham (2001), Basins along the Dead Sea Transform, in *Peri-Tethys Memoir 6: Peri-Tethyan Rift/Wrench Basins and Passive Margins*, edited by W. C. P. A. Ziegler, A.H.F. Robertson, and S. Crasquin-Soleau, *Mem. Mus. Nat. Hist. Nat.*, *186*, 607–627.

Garfunkel, Z., I. Zak, and R. Freund (1981), Active faulting in the Dead Sea Rift, *Tectonophysics*, *80*, 1–26, doi:10.1016/0040-1951(81)90139-6.

Ginat, H., T. Enzel, and Y. Avni (1998), Translocated Plio-Pleistocene drainage systems along the Arava fault of the Dead Sea Transform, *Tectonophysics*, *284*, 151–160, doi:10.1016/S0040-1951(97)00165-0.

Gluck, D. (2002), The landscape evolution of the southwestern Dead Sea Basin and the paleoseismic record of the southwestern marginal fault of the Dead Sea Basin and of the Carmel fault during the Late Pleistocene and the Holocene (in Hebrew with English abstract), *Geol. Surv. Isr. Rep., GSI/4/02*, 86 pp.

Gomez, F., M. Meghraoui, A. N. Darkal, F. Hijazi, M. Mouty, Y. Suleiman, R. Sbeinati, R. Darawcheh, R. Al-Ghazzi, and M. Barazangi (2003), Holocene faulting and earthquake recurrence along the Serghaya branch of the Dead Sea fault system in Syria and Lebanon, *Geophys. J. Int.*, *153*, 658–674, doi:10.1046/j.1365-246X.2003.01933.x.

Gomez, F., G. Karam, M. Khawlie, S. McClusky, P. Vernant, R. Reilinger, R. Jaafar, C. Tabet, K. Khair, and M. Barazangi (2007), Global Positioning System measurements of strain accumulation and slip transfer through the restraining bend along the Dead Sea fault system in Lebanon, *Geophys. J. Int.*, *168*, 1021–1028, doi:10.1111/j.1365-246X.2006.03328.x.

Guidoboni, E., A. Comastri, and G. Traina (1994), *Catalogue of Ancient Earthquakes in the Mediterranean Area up to the 10th Century*, Storia Geofis. Ambiente, Bologna, Italy.

Guidoboni, E., F. Bernardini, A. Comastri, and E. Boschi (2004), The large earthquake on 29 June 1170 (Syria, Lebanon, and central southern Turkey), *J. Geophys. Res.*, *109*, B07304, doi:10.1029/2003JB002523.

Haberland, C., A. Agnon, R. El-Kelani, N. Maercklin, I. Qabbani, G. Rümpker, T. Ryberg, F. Scherbaum, and M. Weber (2003), Modeling of seismic guided waves at the Dead Sea Transform, *J. Geophys. Res.*, *108*(B7), 2342, doi:10.1029/2002JB002309.

Herring, T. A. (1999), Documentation of the GLOBK software version 5.01, report, Mass. Inst. of Technol., Cambridge.

Hofstetter, A., T. Van-Eck, and A. Shapira (1996), Seismic activity along branches of the Dead Sea–Jordan Transform system: The Carmel-Tirtza fault system, *Tectonophysics*, *267*, 317–330, doi:10.1016/S0040-1951(96)00108-4.

Hofstetter, A., H. K. Thio, and G. Shamir (2003), Source mechanism of the 22/11/1995 Gulf of Aqaba earthquake and its aftershock sequence, *J. Seismol.*, *7*, 99–114, doi:10.1023/A:1021206930730.

Hofstetter, R., Y. Klinger, A.-Q. Amrat, L. Rivera, and L. Dorbath (2007), Stress tensor and focal mechanisms along the Dead Sea fault and related structural elements based on seismological data, *Tectonophysics*, *429*, 165–181, doi:10.1016/j.tecto.2006.03.010.

Jacobs, A., D. Sandwell, Y. Fialko, and L. Sichoix (2002), The 1999 (M_w 7.1) Hector Mine, California, earthquake: Near-field postseismic deformation from ERS interferometry, *Bull. Seismol. Soc. Am.*, *92*, 1433–1442, doi:10.1785/0120000908.

Joffe, S., and Z. Garfunkel (1987), Plate kinematics of the circum Red Sea—A re-evaluation, *Tectonophysics*, *141*, 5–22, doi:10.1016/0040-1951(87)90171-5.

Johnson, K. M., and P. Segall (2004), Visco-elastic earthquake cycle models with deep stress-driven creep along the San Andreas fault system, *J. Geophys. Res.*, *109*, B10403, doi:10.1029/2004JB003096.

Kesten, D., M. Weber, C. Haberland, C. Janssen, A. Agnon, Y. Bartov, and I. Rabba (2007), Combining satellite and seismic images to analyse the shallow structure of the Dead Sea Transform near the DESERT transect, *Int. J. Earth Sci.*, *97*, 153–169, doi:10.1007/s00531-006-0168-5.

King, R. W., and Y. Bock (2000), Documentation of the GAMIT GPS analysis software version 9.9, report, Mass. Inst. of Technol., Cambridge.

Klinger, Y., L. Rivera, H. Haessler, and J. Maurin (1999), Active faulting in the Gulf of Aqaba: New knowledge from the M_w 7.3 earthquake of 22 November 1995, *Bull. Seismol. Soc. Am.*, *89*, 1025–1036.

Klinger, Y., J. P. Avouac, N. Abou Karaki, L. Dorbath, D. Bourles, and J. L. Reyss (2000a), Slip rate on the Dead Sea transform fault in northern Araba Valley (Jordan), *Geophys. J. Int.*, *142*, 755–768, doi:10.1046/j.1365-246x.2000.00165.x.

Klinger, Y., J. P. Avouac, L. Dorbath, N. Abou Karaki, and N. Tisnerat (2000b), Seismic behaviour of the Dead Sea fault along Araba Valley, Jordan, *Geophys. J. Int.*, *142*, 769–782, doi:10.1046/j.1365-246x.2000.00166.x.

Klinger, Y., R. Michael, and J.-P. Avouac (2000c), Co-seismic deformation during the M_w 7.3 Aqaba earthquake (1995) from ERS-SAR interferometry, *Geophys. Res. Lett.*, *27*, 3651–3654, doi:10.1029/1999GL008463.

Langbein, J., and H. Johnson (1997), Correlated errors in geodetic time series: Implications for time-dependent deformation, *J. Geophys. Res.*, *102*, 591–603, doi:10.1029/96JB02945.

Magistrale, H. (2002), Relative contributions of crustal temperature and composition to controlling the depth of earthquakes in Southern California, *Geophys. Res. Lett.*, *29*(10), 1447, doi:10.1029/2001GL014375.

Mahmoud, S., R. Reilinger, S. McClusky, P. Vernant, and A. Tealeb (2005), GPS evidence for northward motion of the Sinai Block: Implications for E. Mediterranean tectonics, *Earth Planet. Sci. Lett.*, *238*, 217–224, doi:10.1016/j.epsl.2005.06.063.

Makovsky, Y., A. Wunch, R. Areily, Y. Shaked, A. Rivlin, A. Shemesh, Z. Ben Avraham, and A. Agnon (2008), Quaternary transform kinematics constrained by sequence stratigraphy and submerged coastline features: The Gulf of Aqaba, *Earth Planet. Sci. Lett.*, *271*, 109–122, doi:10.1016/j.epsl.2008.03.057.

Marco, S., T. Rockwell, A. Heimann, and U. Frieslander (2005), Late Holocene slip of the Dead Sea transform revealed in 3D paleoseismic trenches on the Jordan Gorge fault, *Earth Planet. Sci. Lett.*, *234*, 189–205, doi:10.1016/j.epsl.2005.01.017.

Matmon, A., S. Wdowinski, and J. K. Hall (2003), Morphological and structural relations in the Galilee extensional domain, northern Israel, *Tectonophysics*, *371*, 223–241, doi:10.1016/S0040-1951(03)00237-3.

McClusky, S., R. Reilinger, S. Mahmoud, D. Ben Sari, and A. Tealeb (2003), GPS constraints on Africa (Nubia) and Arabia plate motions, *Geophys. J. Int.*, *155*, 126–138, doi:10.1046/j.1365-246X.2003.02023.x.

Meade, B. J., and B. H. Hager (2005), Block models of crustal motion in southern California constrained by GPS measurements, *J. Geophys. Res.*, *110*, B03403, doi:10.1029/2004JB003209.

Meghraoui, M., et al. (2003), Evidence for 830 years of seismic quiescence from palaeoseismology, archaeoseismology and historical seismicity along the Dead Sea fault in Syria, *Earth Planet. Sci. Lett.*, *210*, 35–52, doi:10.1016/S0012-821X(03)00144-4.

Niemi, T. M., H. W. Zhang, M. Atallah, and J. B. J. Harrison (2001), Late Pleistocene and Holocene slip rate of the Northern Wadi Araba fault, Dead Sea Transform, Jordan, *J. Seismol.*, *5*, 449–474, doi:10.1023/A:1011487912054.

Pe'eri, S., S. Wdowinski, A. Shtibelman, N. Bechor, Y. Bock, R. Nikolaidis, and M. van Domselaar (2002), Current plate motion across the Dead Sea fault from three years of continuous GPS monitoring, *Geophys. Res. Lett.*, *29*(14), 1697, doi:10.1029/2001GL013879.

Peltzer, G., P. Rosen, F. Rogez, and K. Hudnut (1998), Proelastic rebound along the Landers 1992 earthquake surface rupture, *J. Geophys. Res.*, *103*, 30,131–30,146, doi:10.1029/98JB02302.

Perfettini, H., and J.-P. Avouac (2004), Stress transfer and strain rate variations during the seismic cycle, *J. Geophys. Res.*, *109*, B06402, doi:10.1029/2003JB002917.

Pollitz, F. (2001), Viscoelastic shear zone model of a strike-slip earthquake cycle, *J. Geophys. Res.*, *106*, 26,541–26,560, doi:10.1029/2001JB000342.

Quennell, A. M. (1958), The Structural and Geomorphic Evolution of the Dead Sea Rift, *Q. J. Geol. Soc. London*, *114*, 1–24.

Regard, V., et al. (2005), Cumulative right-lateral fault slip rate across the Zagros-Makran transfer zone: Role of the Minab-Zendan fault system in accommodating Arabia-Eurasia convergence in southeast Iran, *Geophys. J. Int.*, *162*, 177–203, doi:10.1111/j.1365-246X.2005.02558.x.

Reilinger, R., et al. (2006), GPS constraints on continental deformation in the Africa-Arabia-Eurasia continental collision zone and implications for the dynamics of plate interactions, *J. Geophys. Res.*, *111*, B05411, doi:10.1029/2005JB004051.

Riguzzi, F., G. Pietrantonio, A. Piersanti, and S. M. Mahmoud (2006), Current motion and short-term deformations in the Suez-Sinai area from GPS observations, *J. Geodyn.*, *41*, 485–499, doi:10.1016/j.jog.2006.01.006.

Ron, H., Z. Garfunkel, A. Nur, and R. Freund (1984), Block rotation by strike-slip faulting: Structural and paleomagnetic evidence, *J. Geophys. Res.*, *89*, 6256–6270, doi:10.1029/JB089iB07p06256.

Rotstein, Y., G. Shaliv, and M. Rybakov (2004), Active tectonics of the Yizre'el valley, Israel, using high-resolution seismic reflection data, *Tectonophysics*, *382*, 31–50, doi:10.1016/j.tecto.2003.12.005.

Rybakov, M., V. Goldschmidt, and Y. Rotstein (1997), New regional gravity and magnetic maps of the Levant, *Geophys. Res. Lett.*, *24*, 33–36, doi:10.1029/96GL03617.

Salamon, A., A. Hofstetter, Z. Garfunkel, and H. Ron (1996), Seismicity of the eastern Mediterranean region: Perspective from the Sinai subplate, *Tectonophysics*, *263*, 293–305, doi:10.1016/S0040-1951(96)00030-3.

Salamon, A., A. Hofstetter, Z. Garfunkel, and H. Ron (2003), Seismotectonics of the Sinai subplate—The eastern Mediterranean region, *Geophys. J. Int.*, *155*, 149–173, doi:10.1046/j.1365-246X.2003.02017.x.

Sarti, F., Y. Arkin, J. Chorowicz, A. Karnieli, and T. Cunha (2003), Assessing pre- and post-deformation in the southern Arava Valley segment of the Dead Sea Transform, Israel by differential interferometry, *Remote Sens. Environ.*, *86*, 141–149, doi:10.1016/S0034-4257(03)00066-X.

Savage, J., and R. Burford (1973), Geodetic determination of relative plate motion in central California, *J. Geophys. Res.*, *78*, 832–845, doi:10.1029/JB078i005p00832.

Savage, J. C., J. L. Svarc, and W. H. Prescott (2003), Near-field postseismic deformation associated with the 1992 Landers and 1999 Hector Mine, California, earthquakes, *J. Geophys. Res.*, *108*(B9), 2432, doi:10.1029/2002JB002330.

Sella, G. F., T. H. Dixon, and A. Mao (2002), REVEL: A model for Recent plate velocities from space geodesy, *J. Geophys. Res.*, *107*(B4), 2081, doi:10.1029/2000JB000033.

Shamir, G., G. Baer, and A. Hofstetter (2003), Three-dimensional elastic earthquake modelling based on integrated seismological and InSAR data: The Mw = 7.2 Nuweiba earthquake, gulf of Elat/Aqaba 1995 November, *Geophys. J. Int.*, *154*, 731–744, doi:10.1046/j.1365-246X.2003.01978.x.

Shamir, G., Y. Eyal, and I. Bruner (2005), Localized versus distributed shear in transform plate boundary zones: The case of the Dead Sea Transform in the Jericho Valley, *Geochem. Geophys. Geosyst.*, *6*, Q05004, doi:10.1029/2004GC000751.

Socquet, A., C. Vigny, N. Chamot-Rooke, W. Simons, C. Rangin, and B. Ambrosius (2006), India and Sunda plates motion and deformation along their boundary in Myanmar determined by GPS, *J. Geophys. Res.*, *111*, B05406, doi:10.1029/2005JB003877.

Tapponnier, P., and R. Armijo (1985), Seismotectonics of northern Egypt (abstract), *Terra Cognita*, *5*, 1711985.

Tapponnier, P., M. Daëron, G. King, E. Jacques, A. Sursock, and A. Elias (2001), Active faulting and seismic hazard in Lebanon, *J. Conf. Abstr.*, *6*, EUG XI.

ten Brink, U. S., M. Rybakov, A. S. Al-Zoubi, M. Hassouneh, U. Frieslander, A. T. Batayneh, V. Goldschmidt, M. N. Daoud, Y. Rotstein, and J. K. Hall (1999), Anatomy of the Dead Sea transform: Does it reflect continuous changes in plate motion?, *Geology*, *27*, 887–890, doi:10.1130/0091-7613(1999)027<0887:AOTDST>2.3.CO;2.

Vernant, P., et al. (2004), Present-day crustal deformation and plate kinematics in the Middle East constrained by GPS measurements in Iran and northern Oman, *Geophys. J. Int.*, *157*, 381–398, doi:10.1111/j.1365-246X.2004.02222.x.

Vigny, C., P. Huchon, J.-C. Ruegg, K. Khanbari, and L. M. Asfaw (2006), Confirmation of Arabia plate slow motion by new GPS data in Yemen, *J. Geophys. Res.*, *111*, B02402, doi:10.1029/2004JB003229.

Wdowinski, S., Y. Bock, G. Baer, L. Prawirodirdjo, N. Bechor, S. Naaman, R. Knafo, Y. Forrai, and Y. Melzer (2004), GPS measurements of current crustal movements along the Dead Sea fault, *J. Geophys. Res.*, *109*, B05403, doi:10.1029/2003JB002640.

Williams, S. D. P., Y. Bock, P. Fang, P. Jamason, R. M. Nikolaidis, L. Prawirodirdjo, M. Miller, and D. J. Johnson (2004), Error analysis of continuous GPS position time series, *J. Geophys. Res.*, *109*, B03412, doi:10.1029/2003JB002741.

Zilberman, E., R. Amit, N. Porat, Y. Enzel, and U. Avner (2005), Surface ruptures induced by the devastating 1068 AD earthquake in the southern Arava valley, Dead Sea Rift, Israel, *Tectonophysics*, *408*, 79–99, doi:10.1016/j.tecto.2005.05.030.

A. Agnon, Institute of Earth Sciences, Hebrew University of Jerusalem, Givat Ram, Jerusalem 91904, Israel.

A. Q. Amrat and O. Mayyas, Seismology Division, Natural Resources Authority, P.O. Box 7, Amman 11118, Jordan.

G. Baer, Geological Survey of Israel, 30 Malkhe Yisrael Street, Jerusalem 95501, Israel.

O. Charade, Y. Klinger, M. Le Beon and J.-C. Ruegg, Equipe de Tectonique, Institut de Physique du Globe de Paris, CNRS, 4 Place Jussieu, Box 89, F-75252 Paris CEDEX 05, France. (lebeon@ipgp.jussieu.fr)

L. Dorbath, EOST, 5 rue René Descartes, F-67084 Strasbourg, France.